Hindawi
International Journal of Aerospace Engineering
Volume 2023, Article ID 8872166, 25 pages
https://doi.org/10.1155/2023/8872166

Research Article

Three-Dimensional Guidance Approach with Obstacle Avoidance against Maneuvering Targets

Zi-jie Jiang, Xiu-xia Yang, Yi Zhang, Cong Wang, and Hao Yu

Naval Aviation University, Yantai 264001, China

Correspondence should be addressed to Zi-jie Jiang; 306010136@qq.com

Received 16 December 2022; Revised 6 March 2023; Accepted 8 March 2023; Published 29 March 2023

Academic Editor: Binbin Yan

A guidance approach with obstacle avoidance is proposed for maneuvering target interception. Firstly, by decomposing the constrained optimal guidance problem into two associated subproblems, the overall scheme of guidance is presented. Secondly, to improve the guidance accuracy against the maneuvering target, an MPC controller with disturbance estimation is designed, which transforms the global optimization problem into a finite-horizon optimal control problem. An auxiliary controller is also developed to ensure the system's stability. Then, to achieve obstacle avoidance without affecting the guidance accuracy, a unified function is built to assess the threats from obstacles of different shapes, based on which the optimal guidance-obstacle avoidance model is established. Finally, to solve the above optimization problems, a hybrid solver is developed based on the adaptive moment estimation (Adam) algorithm, whose output will serve as the real-time guidance command. The numerical simulation results show that the guidance approach presented in this paper can achieve precise guidance and obstacle avoidance in various scenarios, and the Monte Carlo experiment further demonstrates the robustness and computation efficiency of the approach.

1. Introduction

To improve the hitting accuracy of interceptors, numerous guidance approaches have been proposed over the decades [1–4]. However, with the increasing complexity of the operational environment, current guidance approaches have gradually shown limitations in the following cases:

(1) To achieve precise guidance when the target is maneuvering

(2) To avoid ground obstacles or enemy threats while pursuing the target

Therefore, the guidance problem involving the above cases has received more attention.

For the former case, some improved guidance methods have been presented for maneuvering target interception, such as the augmented proportional navigation guidance (APNG) law, adaptive sliding-mode guidance (ASMG) law, and optimal guidance law. As an improved proportional navigation guidance (PNG) law, APNG is characterized by its simple form and strong practicability; it restrains the influence of target maneuvers on guidance accuracy by adding the correction term to the law of PNG [5]. Shen [6] derived two forms of APNG, one of which was based on the normal acceleration of target velocity and the other on the angular acceleration of line-of-sight (LOS); however, both of them required the exact target maneuver information that was already known. Besides, APNG cannot overcome the disadvantage that the required overload is overlarge in the endgame of guidance, which may lead to attitude instability during flight. ASMG is an emerging guidance method based on variable structure control theory. It has the advantages of being insensitive to parameter perturbations and resistant to external disturbances. Ji et al. [7] presented a novel time-varying global sliding-mode control

technique using a linear extended state observer to estimate the unknown target acceleration that could achieve maneuvering target interception with the desired impact angle. Authors of [8] proposed a composite three-dimensional guidance law based on an adaptive integral sliding mode control and utilized a nonlinear disturbance observer to estimate and compensate for the disturbances caused by the target maneuver. Although it has been proven to be an advanced method for maneuvering targets during interception [9–13], ASMG still cannot deal with guidance problems with numerous and complex constraints.

With the ability to handle various constraints and objectives, the optimal guidance law has received extensive attention since its explicit formula against maneuvering targets was derived in [14]. Later, Zhang et al. [15] considered the conditions of miss distance, impact angle, terminal angle of attack, etc., and deduced the general formulation of an optimal guidance law by solving the Riccati equation of quadratic optimal control. The authors of [16] provided a unified formulation of optimal guidance-to-collision law for a target with arbitrary acceleration. Weiss and Shima [17] extended optimal guidance theory to the situation where the interceptor had to avoid a spatial region before hitting the target. However, most of the above studies are based on the linear model in the two-dimensional (2D) plane, which reduces the complexity of the problem. Besides, in the derivation of the optimal guidance law, the terminal time is difficult to estimate if the target is maneuvering, which greatly increases the implementation difficulty of these methods. While in model predictive control (MPC) theory, the control action is obtained by solving a finite-horizon open-loop optimal control problem at each sampling instant with no need for knowing the global terminal time, thus making MPC an advantage in solving optimal guidance problems. However, from the current literature, MPC is more used for guidance against stationary targets. For example, in [18], an MPC-based cooperative guidance law is presented to perform a salvo attack against a stationary target in the 2D plane, and in [19], a time-constrained guidance approach for the multimissile network using a nonlinear MPC technique is proposed, which could also achieve the circular no-fly zone avoidance. As an advanced control method capable of resisting external disturbances and system uncertainties, MPC is expected to be further extended to the guidance problem for maneuvering target interception.

As for the latter case, obstacle avoidance has been well studied in the unmanned aerial vehicle (UAV) path planning literature [20–22] but rarely mentioned in guidance research. The essential difference between the two technologies is that the former only needs to lead the UAV to reach a fixed point, while the latter needs to guide the interceptor to hit a rapidly moving target. Precisely because of this difference, some classical obstacle avoidance methods in UAV path planning cannot be directly used for the guidance problem, such as the artificial potential field (APF) method [23]. In APF, the UAV is acted on by the repulsive forces from obstacles and the attractive force from the target, whose resultant force determines the flight direction of the UAV [24]. Among them, the attractive force ensures that, if not affected by any obstacle, the UAV can always aim its flight direction at the target point; this way of keeping the flight direction aimed is also known as the velocity pursuit guidance law (VPGL) in the classical guidance theory [4]. However, VPGL cannot cope with the maneuverability of the target in advance, and when the target has maneuverability not inferior to the interceptor, this kind of guidance strategy will eventually lead to failure in the interception. Similarly, the APF will also face the above difficulty when tackling the guidance problem against maneuvering targets.

In addition to the above, the current guidance literature considering obstacle avoidance is commonly limited to the 2D plane [17, 19, 25], while in a three-dimensional (3D) space, the actual situation is much more complex. Most of the literature on obstacle avoidance in 3D space adopts the method of simplifying obstacle models [26], such as modeling mountains, buildings, and enemy threats into cones, cylinders, hemispheres, and other regular geometries [27], which not only improves computation efficiency but also well describes the geometric characteristics of obstacles. Even so, for obstacles in different shapes, the collision avoidance methods still vary considerably; e.g., in [24], the points of closest are integrated into the 3D APF model to determine the direction and magnitude of repulsive forces; however, the methods to calculate the points of closest are distinct for obstacles in different shapes. In [28], a 3D velocity obstacle (VO) method dedicated to cylindrical obstacles is proposed, which can be a supplement to the 3D VO method developed for spherical obstacles in [29], but neither of them is applicable to avoiding obstacles other than those mentioned above. These methods require the UAV to identify the shapes of obstacles in advance and adopt different ways to avoid them, which increases the difficulty of implementation. A recently proposed method based on fluid flow can cope with obstacles in different shapes while considering maneuverability constraints on the UAV [27]. However, it ensures that the UAV flies to the destination by placing a sink flow at the target point, which is essentially similar to those by constructing the attractive force and will lead to the same difficulty as the APF method encounters in the guidance problem.

In order to solve the guidance problem regarding the above two cases, a guidance approach with obstacle avoidance is proposed for the maneuvering target interception in this paper. The contribution of the manuscript is described in the following: (1) by decomposing the optimal guidance problem with obstacle avoidance constraints into two subproblems associated with the triggering condition, we present the overall scheme of guidance. (2) To make sure the interceptor can accurately hit the target, a MPC controller with improved objective function (to enhance control effect) and an auxiliary controller (to guarantee the system stability) is designed, and an

estimation method is proposed to restrain the system disturbances. Through MPC, the optimal problem with uncertain terminal time is transformed into a finite-horizon optimal control problem. (3) To achieve collision avoidance while changing the optimal guidance command as little as possible, we establish an optimal guidance-obstacle avoidance model, whose objective function contains a threat function built on the VO model, to assess the threats from the obstacles of different shapes. (4) For solving the above two optimization problems, a hybrid solver is developed based on the adaptive moment estimation (Adam) algorithm, whose solution will be used as the guidance command. The rest of the paper is organized as follows. In Section 2, the preliminaries to the guidance geometry and modeling of obstacles are presented, and the overall scheme of guidance with obstacle avoidance is also proposed. Section 3 develops the MPC guidance approach with improved objective function and disturbance estimator. Section 4 presents the guidance-obstacle avoidance approach as well as the hybrid solver. Numerical simulation is performed in Section 5, and finally, the conclusions are drawn in Section 6.

2. Preliminary

2.1. Basic Assumptions. This paper studies the guidance problem with requirements of obstacle avoidance against maneuvering targets, the following assumptions are adopted in the research process:

(1) Both the interceptor and the target are taken as geometric points

(2) Velocities of the interceptor and the target are constants, and only their directions can be changed

(3) The interceptor has ideal dynamic characteristics, the delay of control input is not considered

(4) The obstacles encountered during guidance have been modeled into regular geometries in advance, whose position and geometric characteristics can be acquired

(5) The interceptor can only obtain the position and velocity of the target, the maneuver acceleration or control inputs of the target cannot be measured in advance

2.2. Guidance Geometry. The common coordinate systems to describe guidance problems include the inertial coordinate system, velocity coordinate system, and LOS coordinate system [30]. In this paper, an inertial coordinate system *Oxyz* is established for describing the guidance problem with obstacle avoidance, and the kinematic equations of the interceptor and the target in *Oxyz* are (1) and (2). Figure 1 depicts the movement of the interceptor or the target in the inertial coordinate system.

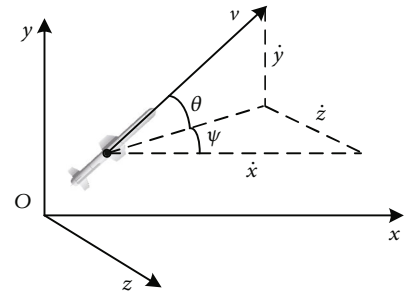

Figure 1: Movement of the interceptor or the target in the inertial coordinate system.

$$\begin{aligned}\dot{x}_{\mathrm{M}} &= v_{\mathrm{M}} \cos\theta_{\mathrm{M}} \cos\psi_{\mathrm{M}},\\ \dot{y}_{\mathrm{M}} &= v_{\mathrm{M}} \sin\theta_{\mathrm{M}},\\ \dot{z}_{\mathrm{M}} &= -v_{\mathrm{M}} \cos\theta_{\mathrm{M}} \sin\psi_{\mathrm{M}},\end{aligned} \tag{1}$$

$$\begin{aligned}\dot{x}_{\mathrm{T}} &= v_{\mathrm{T}} \cos\theta_{\mathrm{T}} \cos\psi_{\mathrm{T}},\\ \dot{y}_{\mathrm{T}} &= v_{\mathrm{T}} \sin\theta_{\mathrm{T}},\\ \dot{z}_{\mathrm{T}} &= -v_{\mathrm{T}} \cos\theta_{\mathrm{T}} \sin\psi_{\mathrm{T}},\end{aligned} \tag{2}$$

wherein, the subscript M and T, respectively, denote the interceptor and the target, whose inclination angles are θ_{M} and θ_{T}, deflection angles are ψ_{M} and ψ_{T}, and space velocities are v_{M} andv_{T}.

The state vector of the guidance system is chosen as

$$\boldsymbol{\chi} = [\chi_1, \chi_2, \cdots, \chi_{10}]^{\mathrm{T}} = [x_{\mathrm{M}}, y_{\mathrm{M}}, z_{\mathrm{M}}, \theta_{\mathrm{M}}, \psi_{\mathrm{M}}, x_{\mathrm{T}}, y_{\mathrm{T}}, z_{\mathrm{T}}, \theta_{\mathrm{T}}, \psi_{\mathrm{T}}]^{\mathrm{T}}. \tag{3}$$

Then, the nonlinear system can be described by the state equation:

$$\dot{\boldsymbol{\chi}}(t) = \boldsymbol{f}(\boldsymbol{\chi}(t), \boldsymbol{u}(t), \boldsymbol{w}(t)), \tag{4}$$

$$\boldsymbol{f}(\boldsymbol{\chi}(t), \boldsymbol{u}(t), \boldsymbol{w}(t)) = \begin{bmatrix} v_{\mathrm{M}} \cos\chi_4(t) \cos\chi_5(t) \\ v_{\mathrm{M}} \sin\chi_4(t) \\ -v_{\mathrm{M}} \cos\chi_4(t) \sin\chi_5(t) \\ u_1(t) \\ u_2(t) \\ v_{\mathrm{T}} \cos\chi_9(t) \cos\chi_{10}(t) \\ v_{\mathrm{T}} \sin\chi_9(t) \\ -v_{\mathrm{T}} \cos\chi_9(t) \sin\chi_{10}(t) \\ w_1(t) \\ w_2(t) \end{bmatrix}, \tag{5}$$

where the control input vector $\boldsymbol{u}(t) = [u_1(t), u_2(t)]^{\mathrm{T}} =$

$[\dot{\theta}_M(t), \dot{\psi}_M(t)]^T$ consists of the inclination angular velocity and the deflection angular velocity of the interceptor. Accordingly, the system disturbance caused by the target maneuver can be denoted as $\boldsymbol{w}(t) = [w_1(t), w_2(t)]^T = [\dot{\theta}_T(t), \dot{\psi}_T(t)]^T$. The aim of guidance is to make the distance between both sides shown in Equation (6) as small as possible at the end of the guidance.

$$r(\boldsymbol{\chi}(t)) = \sqrt{\sum_{i=1}^{3} (\chi_i - \chi_{i+5})^2}. \tag{6}$$

2.3. Modeling of Obstacles. To avoid obstacles during guidance, an efficient modeling method is first needed. In this paper, all the obstacles or enemy threat regions are treated as regular geometries. For example, the mountains are taken as cones, the buildings as cylinders, and the coverage areas of enemy radars as hemispheres. To ensure the flight safety of the interceptor, those geometries could suitably envelop the obstacles with keeping a certain margin (safe distance) [27]. Their unified model can be described with Equations (7) and (8).

Remark 1. For the convenience of expression, all the obstacles, threat regions, and the regular geometries they are treated as, are collectively referred to as obstacles.

$$\Gamma_i(x, y, z) = (x - x_{oi})^2 + (z - z_{oi})^2 - \varsigma(\boldsymbol{\omega}_i, y), \tag{7}$$

$$\varsigma(\boldsymbol{\omega}_i, y) = \omega_{i1} y^2 + \omega_{i2} y + \omega_{i3}, \tag{8}$$

where $\mathcal{O} = \{o_i | i = 1, \cdots n_o\}$ is the set of obstacles, (z_{oi}, x_{oi}) is the projection of the geometric center of o_i on the plane z Ox, and the parameter $\boldsymbol{\omega}_i$ is related to the shape of o_i.

And there is

$$(x, y, z) \begin{cases} \text{inside } o_i & \Gamma_i(x, y, z) < 0 \wedge 0 < y < H_i \\ \text{outside } o_i & \text{else} \end{cases}. \tag{9}$$

H_i is the height of o_i.

For the above three typical geometries, the relationship between their shapes and parameter $\boldsymbol{\omega}_i$ is shown in Figure 2.

Remark 2. The obstacle avoidance method developed in this paper is applicable to all the obstacles that can be described with Equations (7) and (8), while the above three are only the typical ones among them, which are introduced to facilitate the analysis in the following parts.

2.4. Optimization Model of Guidance with Obstacle Avoidance Constraints. On the basis of the above, the optimal guidance problem with obstacle avoidance constraints can be expressed as Problem 3.

Problem 3. Given the initial system states $\boldsymbol{\chi}(t_0)$, find

$$\boldsymbol{u}^*(t) = \arg \min_{\boldsymbol{u}(t)} r(\boldsymbol{\chi}(t_f), \boldsymbol{u}(t), \boldsymbol{w}(t)), \tag{10}$$

subject to

$$\boldsymbol{u}(t) \in \mathcal{U}, \tag{11}$$

$$\Gamma_i(\chi_1(t), \chi_2(t), \chi_3(t)) > 0, \tag{12}$$

$$\dot{r}(\boldsymbol{\chi}(t_f)) = 0. \tag{13}$$

Herein, t_0 and t_f are the initial time and the terminal time of guidance, $\mathcal{U} = \{[u_1, u_2]^T | |u_i| \le U_{\max i}, i = 1, 2\}$ is the input constraint set, Equation (12) is the obstacle avoidance constraint, and Equation (13) is the terminal condition of guidance.

Remark 4. During guidance, the time derivative of r is always negative, which means the distance between the interceptor and the target constantly decreases. Once $\dot{r}$ reaches zero, implying that r will no longer decrease, then the guidance ends immediately [17], so Equation (13) can be taken as the terminal condition of guidance, which also helps to determine the terminal time and terminal miss distance.

2.5. Overall Scheme of Guidance with Obstacle Avoidance. To solve the above optimal guidance problem, the following issues should be considered first:

(a) The obstacle avoidance constraint (12) is difficult to handle

(b) Terminal time t_f is hard to get unless the future maneuver information of the target is fully known

Regarding a, a general way to deal with nonlinear constraints is by adding a penalty term to the objective function [19]. The modified function will have the form of

$$\tilde{J}(\boldsymbol{\chi}(t), \boldsymbol{u}(t)) = J_1(\boldsymbol{\chi}(t), \boldsymbol{u}(t), \boldsymbol{w}(t)) + \mu J_2(\boldsymbol{\chi}(t), \boldsymbol{u}(t)), \tag{14}$$

where $J_1(\boldsymbol{\chi}(t), \boldsymbol{u}(t), \boldsymbol{w}(t)) = r(\boldsymbol{\chi}(t_f), \boldsymbol{u}(t), \boldsymbol{w}(t))$, $J_2(\bullet)$ is the cost function constructed on the obstacle avoidance constraint (12), μ is the weight coefficient that affects both the guidance accuracy and the success rate of obstacle avoidance.

However, in order to guarantee the flight safety of the interceptor, the value of μ must be large enough to deal with the possibility that J_2 is much smaller than J_1 in the initial phase of guidance. As a result, any trivial change of J_2 will greatly impact the guidance command in the endgame, which may lead to the failure of interception.

To tackle the above issue, we decompose the optimal Problem 3 with constraint (12) into two subproblems, which are shown below.

Problem 5. Given the initial system states $\boldsymbol{\chi}(t_0)$, find

$$\boldsymbol{u}^*(t) = \arg \min_{\boldsymbol{u}(t)} J_1(\boldsymbol{\chi}(t), \boldsymbol{u}(t), \boldsymbol{w}(t)), \tag{15}$$

subject to (11).

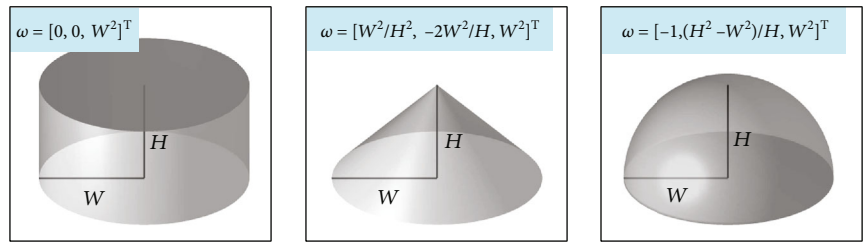

Figure 2: Three typical geometries of obstacle and their parameters.

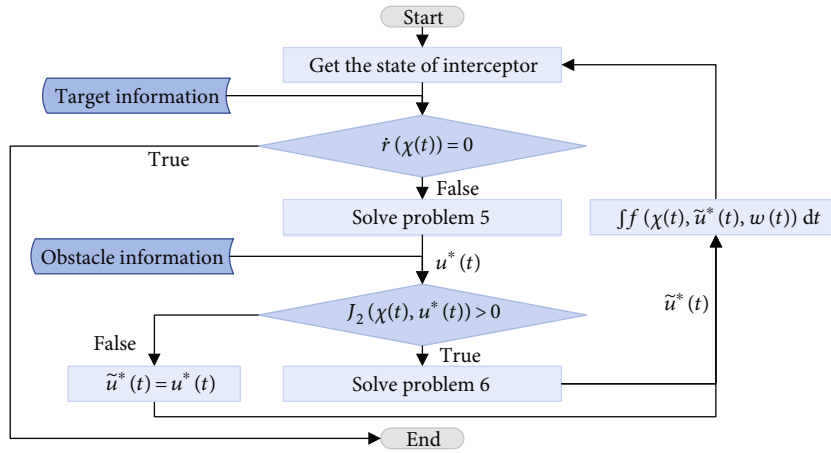

Figure 3: Overall scheme of guidance with obstacle avoidance.

Problem 6. Given the system states $\chi(t)$ and guidance command$\boldsymbol{u}^*(t)$, find

$$\tilde{\boldsymbol{u}}^*(t) = \arg \min_{\tilde{\boldsymbol{u}}(t)} \|\tilde{\boldsymbol{u}}(t) - \boldsymbol{u}^*(t)\|_p + J_2(\chi(t), \tilde{\boldsymbol{u}}(t)), \quad (16)$$

subject to

$$\tilde{\boldsymbol{u}}(t) \in \mathcal{U}, \quad (17)$$

$$J_2(\chi(t), \boldsymbol{u}^*(t)) > 0. \quad (18)$$

Here, the optimal solution to Problem 5 will be the guidance command in cases where the interceptor does not need to avoid any obstacle. Inequality (18) serves as a triggering condition, once it holds, the interceptor needs to change its present guidance command (by solving Problem 6) lest colliding with obstacles. The objective function of Problem 6 consists of the p-norm of $\tilde{\boldsymbol{u}}(t) - \boldsymbol{u}^*(t)$ and the cost function of obstacle avoidance, to ensure the guidance command is changed as little as possible when the obstacles are avoided. In this way, the overall scheme of guidance with obstacle avoidance can be shown in Figure 3. In the following sections, we will analyze the above two problems, respectively.

As for *b*, with the existence of system disturbances caused by the target maneuver, it is difficult to calculate the terminal time t_f. While model predictive control (MPC) has good adaptability to this kind of optimal control problems with uncertain terminal time, by transforming them into optimal control problems with certain optimization horizons. Consequently, to get the optimal guidance command $\boldsymbol{u}^*(t)$ from Problem 5, a guidance approach based on MPC is proposed in Section 3.

3. MPC Guidance Approach

In this section, the optimal guidance Problem 5 will be redefined as a finite-horizon optimal control problem (FHOCP) under the MPC framework. To improve the guidance performance while ensuring the system's stability, an objective function based on ZEM and an auxiliary controller are designed. An estimation method is also proposed to restrain the system disturbances. By solving FHOCP Problem 12, we can get $\boldsymbol{u}^*(k)$ at each instant.

3.1. Nonlinear MPC. As noted in the introduction, the control action of MPC is obtained at each sampling instant, thus the system description of MPC is commonly based on a discrete model. Using the Euler method, we can discretize system (5) into

$$\chi(k+1) = \boldsymbol{F}(\chi(k), \boldsymbol{u}(k), \boldsymbol{w}(k)) \quad (19)$$

where δ is the sampling period of the discrete system.

At sampling instant k (corresponding to the actual time $t_0 + k\delta$), $k = 0, 1, \cdots$, given the initial system states $\chi(k)$, control input sequence $\boldsymbol{u}(k), \cdots, \boldsymbol{u}(k+P-1)$, and system disturbances $\boldsymbol{w}(k), \cdots, \boldsymbol{w}(k+P-1)$, we can get the system

states within the prediction horizon.

$$\boldsymbol{\chi}(k+l) = \boldsymbol{F}(\boldsymbol{\chi}(k+l-1), \boldsymbol{u}(k+l-1), \boldsymbol{w}(k+l-1)), l = 1, \cdots, P, \tag{20}$$

where $P \in \mathbb{Z}^+$ is the length of the prediction horizon.

Then, Problem 5 can be redefined as a FHOCP, i.e.,

Problem 7. Given the initial system states $\boldsymbol{\chi}(k)$, find the optimal control input sequence

$$\boldsymbol{u}^*(P;k) = \arg \min_{\boldsymbol{u}(P;k)} J_1(k, \boldsymbol{\chi}(P;k), \boldsymbol{u}(P;k), \boldsymbol{w}(P;k)), \tag{21}$$

subject to (20) and

$$\boldsymbol{u}(P;k) \in \boldsymbol{\mathcal{U}}., \tag{22}$$

After obtaining the optimal control input sequence at the sampling instant k, we apply its first component to the actual system. When the time comes to the next instant $k+1$, we will observe the system states and solve another FHOCP. The above process will be repeated until the end of the control.

Due to the real-time observation and correction, MPC can deal with external disturbances and model uncertainty, and in the rest of this section, our focus will be on the design of the MPC controller.

3.2. Improved Objective Function Based on ZEM. Traditionally, the objective function of MPC consists of two parts, one is called the stage cost function which describes the aim of control, and the other is terminal cost function that guarantees the stability of the system. In the design of the stage cost function, we introduce an approximation of the terminal miss distance, i.e., zero-effort-miss (ZEM). ZEM plays an essential role in some existing literatures [31, 32], it implies the assumption about the future motion of the interceptor and the target, rather than just focusing on their current positions. Then, based on the stage cost function, we design the terminal cost function and its associated auxiliary controller to ensure recursive feasibility and system stability. A detailed analysis of the convergence can be seen in the appendix.

For ease of design, we introduce new state variables as

$$\boldsymbol{r} = \begin{bmatrix} r_x \\ r_y \\ r_z \end{bmatrix} = \begin{bmatrix} \chi_1 - \chi_6 \\ \chi_2 - \chi_7 \\ \chi_3 - \chi_8 \end{bmatrix}. \tag{23}$$

Definition 8 Zero-effort-miss (ZEM) [33]. The distance that the interceptor would miss the target provided that the target continued along its present course, and the interceptor made no further corrective maneuver.

According to Definition 8, we derive the analytical formula of ZEM in an inertial coordinate system as

$$\tilde{r} = \sqrt{\frac{(r_x\dot{r}_y - r_y\dot{r}_x)^2 + (r_x\dot{r}_z - r_z\dot{r}_x)^2 + (r_y\dot{r}_z - r_z\dot{r}_y)^2}{\dot{r}_x{}^2 + \dot{r}_y{}^2 + \dot{r}_z{}^2}}. \tag{24}$$

And the estimation of terminal time based on ZEM is formulated as

$$t_{\text{go}} = \frac{\dot{r}_x r_x + \dot{r}_y r_y + \dot{r}_z r_z}{\dot{r}_x{}^2 + \dot{r}_y{}^2 + \dot{r}_z{}^2}. \tag{25}$$

The derivation process follows that in the situation of Definition 8, the change of distance between the interceptor and the target with respect to time is

$$r(t) = \sqrt{(r_x + \dot{r}_x t)^2 + (r_y + \dot{r}_y t)^2 + (r_z + \dot{r}_z t)^2}. \tag{26}$$

According to the extremum formula of the quadratic function, we can get the extreme point of $r(t)$ as t_{go}, and the extreme value as $\tilde{r}$.

Remark 9. When $t_{\text{go}} \le \delta$, both the interceptor and the target will stop control and fly to the terminal point in their instantaneous attitudes. For this situation, $\dot{r}(t_{\text{go}})$ will be 0, and ZEM will be equal to the actual terminal miss distance. Therefore, to obtain the actual guidance effect, we reset δ to t_{go} if there is $t_{\text{go}} \le \delta$ (see Section 5).

Let $L = (r_x\dot{r}_y - r_y\dot{r}_x)^2 + (r_x\dot{r}_z - r_z\dot{r}_x)^2 + (r_y\dot{r}_z - r_z\dot{r}_y)^2$. Then, we define the stage cost function as

$$J_{\text{S}}(k, \boldsymbol{\chi}(P;k), \boldsymbol{u}(P;k), \boldsymbol{w}(P;k)) = \sum_{l=0}^{P-1} L(\boldsymbol{\chi}(k+l)). \tag{27}$$

To guarantee the recursive feasibility and stability of the system, the terminal cost function and the auxiliary controller are designed as follows.

Terminal cost function

$$J_{\text{T}}(k, \boldsymbol{\chi}(k+P), \boldsymbol{u}(P;k), \boldsymbol{w}(P;k)) = \rho \cdot L(\boldsymbol{\chi}(k+P)), \tag{28}$$

where $\rho > 1, \rho \in \mathbb{R}$.

Auxiliary controller

$$\boldsymbol{u}_\kappa = \begin{bmatrix} u_{\kappa 1} \\ u_{\kappa 2} \end{bmatrix} = \begin{bmatrix} \dfrac{K_1 \cos\chi_5 + K_2 \sin\chi_5}{r_x\dot{\chi}_1 + r_y\dot{\chi}_2 + r_z\dot{\chi}_3} \\ \dfrac{K_1 \sin\chi_5 - K_2 \cos\chi_5 + (r_x\dot{\chi}_3 - r_z\dot{\chi}_1)u_{\kappa 1}}{r_y v_{\text{M}} \cos\chi_4} \end{bmatrix}. \tag{29}$$

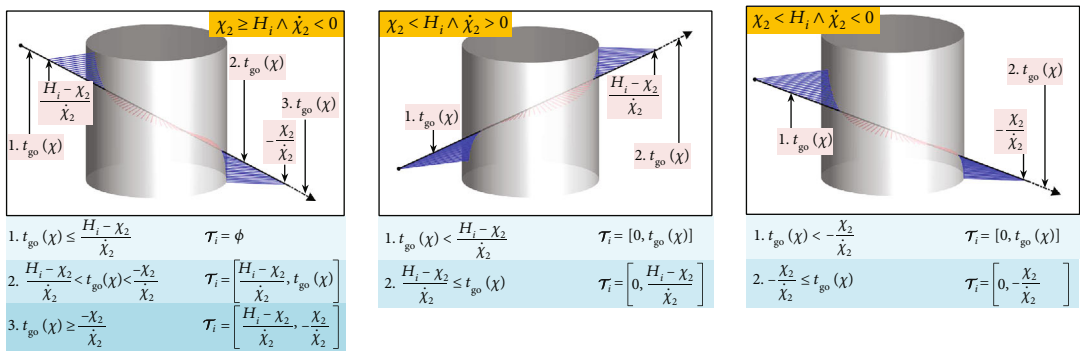

Figure 4: Situations related to the feasible range of time.

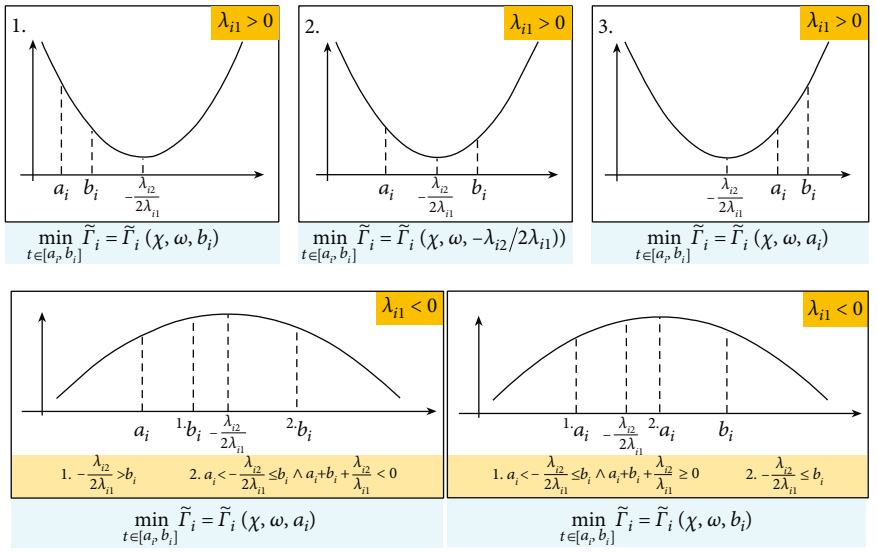

Figure 5: Several situations regarding the value of threat function.

In which

$$\boldsymbol{K} = \begin{bmatrix} K_1 \\ K_2 \end{bmatrix} = \begin{bmatrix} -\lambda\left(r_x\dot{r}_y - r_y\dot{r}_x\right) + r_x\tilde{w}_y - r_y\tilde{w}_x \\ -\lambda\left(r_y\dot{r}_z - r_z\dot{r}_y\right) + r_y\tilde{w}_z - r_z\tilde{w}_y \end{bmatrix}, \tag{30}$$

$$\lambda > 1/2(\rho - 1)\delta, \lambda \in \mathbb{R},$$

$$\tilde{\boldsymbol{w}} = \begin{bmatrix} \tilde{w}_x \\ \tilde{w}_y \\ \tilde{w}_z \end{bmatrix} = v_T \cdot \begin{bmatrix} -\sin\chi_9\cos\chi_{10} & -\cos\chi_9\sin\chi_{10} \\ \cos\chi_9 & 0 \\ \sin\chi_9\sin\chi_{10} & -\cos\chi_9\cos\chi_{10} \end{bmatrix} \cdot \boldsymbol{w}. \tag{31}$$

And we assume that by changing the value of λ, there always exist $\boldsymbol{u}_\kappa(k) \in \mathcal{U}$ at any $k > 0$.

Then, given (27) and (28), the objective function at instant k can be defined as

$$J_1(k, \boldsymbol{\chi}(P;k), \boldsymbol{u}(P;k), \boldsymbol{w}(P;k)) = J_S(k, \boldsymbol{\chi}(P;k), \boldsymbol{u}(P;k), \boldsymbol{w}(P;k)) + J_T(k, \boldsymbol{\chi}(k+P), \boldsymbol{u}(P;k), \boldsymbol{w}(P;k)). \tag{32}$$

For ease of description, we abbreviate $J_1(k, \boldsymbol{\chi}(P;k), \boldsymbol{u}(P;k), \boldsymbol{w}(P;k))$ as $J_1(k)$ and $J_T(k, \boldsymbol{\chi}(k+P), \boldsymbol{u}(P;k), \boldsymbol{w}(P;k))$ as $J_T(k+P|k)$ in the following sections. Accordingly, the optimal value of the objective function at instant k is denoted as $J_1^*(k)$.

Remark 10. The auxiliary controller does not act on the actual system in the initial phase of guidance, its true role is as the component of the initial solution for each iteration (which will be clarified in the proof), and the actual control action is still obtained by solving the FHOCP. Once J_1 converges to zero, the subsequent control actions will be generated by the auxiliary controller.

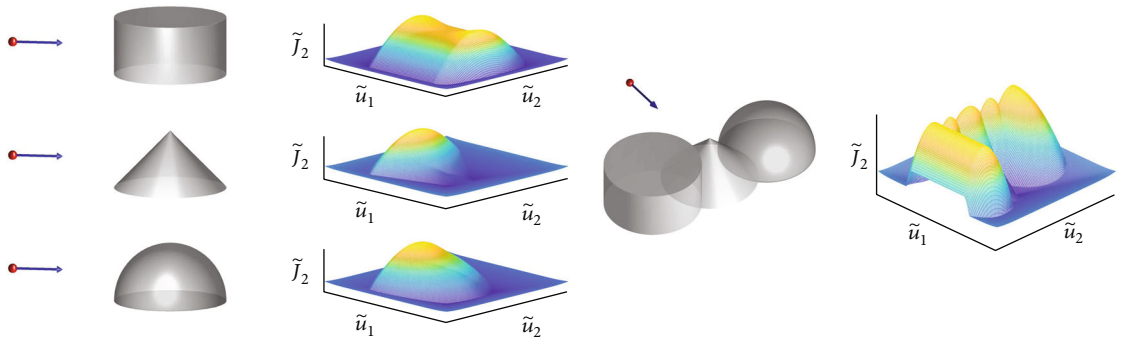

Figure 6: Function images of $\tilde{J}_2$ in several situations.

1: **// Adam for Problem12**
2: **// Initialization**
3: Set the parameters of the algorithm:
$\bar{K}_1$, K_1, β_1, β_2, α
4: Generate initial solution $\boldsymbol{u}^{(0)}(P;k)$ using (63)
5: Initialize first and second moment estimates, initialize iteration as iter = 0
6: **// Main loop**
7: **while**$\kappa < \bar{K}_1 \wedge \text{iter} < K_1$**do**
8: Calculate $J_1(\boldsymbol{u}^{(\text{iter})}(P;k))$ using (49), calculate κ using (73)
9: Update $\boldsymbol{u}^{(\text{iter})}(P;k)$ using (65)–(70)
10: Correct $\boldsymbol{u}^{(\text{iter})}(P;k)$ using (72)
11: Update current iteration as iter = iter + 1
12: **end while**
13: Determine the optimal solution $\boldsymbol{u}^*(P;k)$ using (76), take the first components as $\boldsymbol{u}^*(k)$
14: **// Determine whether**$\boldsymbol{u}^*(k)$**could serve as eventual guidance command**
15: Calculate $J_2(\boldsymbol{u}^*(k))$
16: **if**$J_2(\boldsymbol{u}^*(k)) = 0$**then**
17: Determine eventual guidance command as $\tilde{\boldsymbol{u}}^*(k) = \boldsymbol{u}^*(k)$
18: **else**
19: **// Adam for Problem14**
20: **// Initialization**
21: Set the parameters of the algorithm: $\bar{K}_2$, K_2
22: Generate initial solution $\tilde{\boldsymbol{u}}_j^{(0)}$, $j = 1, \cdots, N_{\text{P}}$ using (64)
23: **// Main loop**
24: **for**j:=1 to N_{P}**do**
25: Initialize first and second moment estimates, initialize iteration as $iter = 0$
26: **while**$\kappa < \bar{K}_2 \wedge \text{iter} < K_2$**do**
27: Calculate $\tilde{J}_2(\tilde{\boldsymbol{u}}_j^{(iter)})$ using (59), calculate κ using (73)
28: Update $\tilde{\boldsymbol{u}}_j^{(iter)}$ using (65)–(70)
29: Correct $\tilde{\boldsymbol{u}}_j^{(iter)}$ using (72)
30: Update the current iteration as iter = iter + 1
31: **end while**
32: Determine the optimal individual $\tilde{\boldsymbol{u}}_j^*$ using (76)
33: **end for**
34: Determine the optimal solution $\tilde{\boldsymbol{u}}^*(k)$ using (77)
35: **// Results**
36: **return**$\tilde{\boldsymbol{u}}^*(k)$

Algorithm 1: Pseudocode of the hybrid solver.

Next, we will analyze the convergence of the system under the action of the MPC controller, by giving Theorem 11 and its proof.

Theorem 11. *Let the terminal cost function be given as in (28), then, by introducing the auxiliary controller (29), the optimal value of the objective function will decrease to zero.*

Proof. The proof follows that by constructing a feasible solution in an instant k, as shown in

$$\widehat{\boldsymbol{u}}(P;k)=\begin{cases}\boldsymbol{u}^{*}(k+l|k-1), & l=0,\cdots,P-2,\\ \boldsymbol{u}_{\kappa}(k+l), & l=P-1.\end{cases} \tag{33}$$

We can prove that the objective function value of $\widehat{\boldsymbol{u}}(P;k)$ meets $J_1(k)\le J_1{}^{*}(k-1)$, and there must be $J_1{}^{*}(k)\le J_1(k)\le J_1{}^{*}(k-1)$, so the requirement in Theorem 11 is guaranteed. For more details, see the appendix. □

3.3. Disturbance Estimation Based on Historical Data. Prior to solving the above finite-horizon optimal Problem 7, we need to know the system disturbances within the prediction horizon, that is $\boldsymbol{w}(P;k)$. However, since future disturbances caused by the target maneuver cannot be measured in advance, we can only predict them by finding the existing laws in the historical data. Fitting extrapolation is a common method in target trajectory prediction [34, 35], whose basic idea is to use the preestablished models or functions to approximate the historical data and predict the future motion of the target with the fitted model. Based on the fitting extrapolation, we propose a disturbance estimation method for short-term prediction and specify its implementation at each instant. The estimation results can be used for the MPC controller designed above.

Considering that the disturbances caused by the target maneuver cannot be directly measured, the estimated objects are chosen as

$$\boldsymbol{e}(k)=\begin{bmatrix}e_1(k)\\ e_2(k)\end{bmatrix}=\frac{1}{\delta}\begin{bmatrix}\chi_9(k+1)-\chi_9(k)\\ \chi_{10}(k+1)-\chi_{10}(k)\end{bmatrix}. \tag{34}$$

The following assumption related to the estimated objects is adopted in the derivation process.

Assumption 12. The estimated object

(1) is n-order differentiable with respect to time, and there is $e_i{}^{(n)}=\sum_{j=0}^{n-1}b_{ji}e_i{}^{(j)}$, $i=1,2$

Assumption 13. Itself and its derivatives of any order are bounded, i.e., $|e_i^{(j)}(t)|\le d_{ij}$.

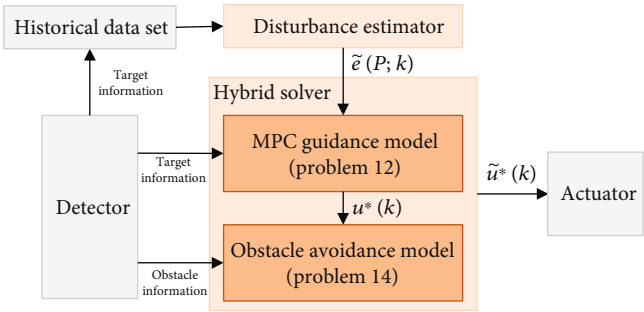

Figure 7: Implementation of the guidance approach with obstacle avoidance.

Based on Assumption (12), we obtain an autonomous linear system which can be described with

$$\begin{aligned}\dot{\boldsymbol{\gamma}}_i&=\boldsymbol{A}_i\boldsymbol{\gamma}_i,\\ e_i&=\boldsymbol{C}\boldsymbol{\gamma}_i,\end{aligned} \tag{35}$$

where

$$\boldsymbol{A}_i=\begin{bmatrix}\boldsymbol{0} & \boldsymbol{I}_{n-1}\\ b_{0i} & b_{1i}\cdots b_{n-1,i}\end{bmatrix}, \tag{36}$$

$\boldsymbol{C}=[1\quad 0\quad \cdots\quad 0]$ and $\boldsymbol{\gamma}_i\triangleq[e_i,\dot{e}_i,\cdots,e_i^{(n-1)}]^{\mathrm{T}}$.

The state response of system (35) from zero moments to time t is formulated as

$$\boldsymbol{\gamma}_i(t)=\mathrm{e}^{\boldsymbol{A}_i t}\boldsymbol{\gamma}_{i0}. \tag{37}$$

Herein, $\boldsymbol{\gamma}_{i0}=\boldsymbol{\gamma}_i(0)$. It also can be derived from Equation (37) that $e_i(t)=\boldsymbol{C}\mathrm{e}^{\boldsymbol{A}_i t}\boldsymbol{\gamma}_{i0}$ and $e_i^{(j)}(t)=\boldsymbol{C}\boldsymbol{A}_i{}^{j}\mathrm{e}^{\boldsymbol{A}_i t}\boldsymbol{\gamma}_{i0}$.

Using Taylor's formula, we obtain

$$e_i(t)=\sum_{j=0}^{\infty}\frac{t^j}{j!}\boldsymbol{C}\boldsymbol{A}_i{}^{j}\boldsymbol{\gamma}_{i0}=\sum_{j=0}^{n-1}\frac{t^j}{j!}\boldsymbol{C}\boldsymbol{A}_i{}^{j}\boldsymbol{\gamma}_{i0}+R_{n-1}(t), \tag{38}$$

where $R_{n-1}(t)$ is the Lagrange remainder which satisfies $R_{n-1}(t)=(t^n/n!)e_i{}^{(n)}(\tilde{t})$, $\tilde{t}$ lies between 0 and t. So we can draw from Equation (38), if t is in the neighborhood of 0, $e_i(t)$ can be approximated by a polynomial function $g_i(\boldsymbol{\alpha}_i,t)=\sum_{j=0}^{n}\alpha_{ij}t^j$.

Then, to determine the fitting coefficients $\boldsymbol{\alpha}_i=[\alpha_{i0},\cdots,\alpha_{i,n-1}]^{\mathrm{T}}$, we need to utilize the historical data.

Bringing in data $(t_1,e_i(t_1))$, $\cdots$, $(t_q,e_i(t_q))$, and $t_j\ne t_l$ if $j\ne l$ and $q>n$, we can get the least-squares solution of the equation $\boldsymbol{\Gamma}_i\boldsymbol{\alpha}_i=\boldsymbol{e}_i$, that is

$$\boldsymbol{\alpha}_i{}^{*}=\boldsymbol{\Gamma}_i{}^{-}\boldsymbol{e}_i. \tag{39}$$

Table 1: Shapes and positions of obstacles in example 1.

	Shape	Projection of geometric center on zOx (m)	Half of bottom width (m)	Height (m)
Case 1	Cylinder	(700,800)	300	500
Case 2	Cone	(700,800)	400	600
Case 3	Hemisphere	(700,800)	400	400

Table 2: The initial states of the interceptor and the target in example 1.

	x(m)	y(m)	z(m)	$\theta(\pi$ rad)	$\psi(\pi$ rad)	v(m/s)
Interceptor	0	300	0	0	-1/4	40
Target	2000	300	2000	0	3/4	30

Herein,

$$\boldsymbol{\Gamma}_i = \begin{bmatrix} 1 & t_1 & \cdots & t_1^{n-1} \\ \vdots & \vdots & & \vdots \\ 1 & t_q & \cdots & t_q^{n-1} \end{bmatrix}, \tag{40}$$

$\boldsymbol{e}_i = [e_i(t_1),\cdots,e_i(t_q)]^{\mathrm{T}}$, and $\boldsymbol{\Gamma}_i^- = (\boldsymbol{\Gamma}_i^{\mathrm{T}}\boldsymbol{\Gamma}_i)^{-1}\boldsymbol{\Gamma}_i^{\mathrm{T}}$ are the left inverse of matrix $\boldsymbol{\Gamma}_i$. Then the fitting function can be noted as $g_i(\boldsymbol{\alpha}_i^*,\cdot)$.

The fitting error is represented in the form of matrix

$$\begin{aligned} \boldsymbol{\varepsilon}_i &= \left[g_i(\boldsymbol{\alpha}_i^*,t_1) - e_i(t_1),\cdots,g_i\left(\boldsymbol{\alpha}_i^*,t_q\right) - e_i\left(t_q\right)\right]^{\mathrm{T}} \\ &= \boldsymbol{\Gamma}_i\boldsymbol{\alpha}_i^* - \boldsymbol{e}_i = (\boldsymbol{\Gamma}_i\boldsymbol{\Gamma}_i^- - \boldsymbol{I})\boldsymbol{e}_i = (\boldsymbol{\Gamma}_i\boldsymbol{\Gamma}_i^- - \boldsymbol{I})(\boldsymbol{\Gamma}_i\boldsymbol{\phi}_i + \boldsymbol{R}_i) \\ &= \boldsymbol{\Gamma}_i\boldsymbol{\Gamma}_i^-\boldsymbol{\Gamma}_i\boldsymbol{\phi}_i - \boldsymbol{\Gamma}_i\boldsymbol{\phi}_i + \boldsymbol{\Gamma}_i\boldsymbol{\Gamma}_i^-\boldsymbol{R}_i - \boldsymbol{R}_i = \boldsymbol{\Gamma}_i\boldsymbol{\Gamma}_i^-\boldsymbol{R}_i - \boldsymbol{R}_i. \end{aligned} \tag{41}$$

Further, there is

$$\boldsymbol{R}_i = (\boldsymbol{\Gamma}_i\boldsymbol{\Gamma}_i^- - \boldsymbol{I})^{-1}\boldsymbol{\varepsilon}_i, \tag{42}$$

where

$$\begin{aligned} \boldsymbol{\phi}_i &= \left[\boldsymbol{C}\boldsymbol{\gamma}_{i0}, \boldsymbol{C}\boldsymbol{A}_i\boldsymbol{\gamma}_{i0},\cdots,\frac{\boldsymbol{C}\boldsymbol{A}_i^{(n-1)}\boldsymbol{\gamma}_{i0}}{(n-1)!}\right]^{\mathrm{T}}, \\ \boldsymbol{R}_i &= \left[R_{n-1}(t_1),\cdots,R_{n-1}\left(t_q\right)\right]^{\mathrm{T}}. \end{aligned} \tag{43}$$

If we use $g_i(\boldsymbol{\alpha}_i^*,\cdot)$ to estimate $e_i(t)$, t is not among t_1, $\cdots$, t_q, the estimation error will be as shown in

$$\begin{aligned} \tilde{\varepsilon}_i(t) &= \left[1,t,\cdots,t^{n-1}\right]\cdot\boldsymbol{\alpha}_i^* - e_i(t) = \left[1,t,\cdots,t^{n-1}\right]\cdot\boldsymbol{\Gamma}_i^-\boldsymbol{e}_i - e_i(t) \\ &= \left[1,t,\cdots,t^{n-1}\right]\cdot\boldsymbol{\Gamma}_i^-(\boldsymbol{\Gamma}_i\boldsymbol{\phi}_i + \boldsymbol{R}_i) - \left[1,t,\cdots,t^{n-1}\right]\cdot\boldsymbol{\phi}_i - R_{n-1}(t) \\ &= \left[1,t,\cdots,t^{n-1}\right]\cdot\boldsymbol{\Gamma}_i^-\boldsymbol{R}_i - R_{n-1}(t) = \left[1,t,\cdots,t^{n-1}\right] \\ &\quad\cdot\boldsymbol{\Gamma}_i^-(\boldsymbol{\Gamma}_i\boldsymbol{\Gamma}_i^- - \boldsymbol{I})^{-1}\varepsilon_i - R_{n-1}(t) \end{aligned} \tag{44}$$

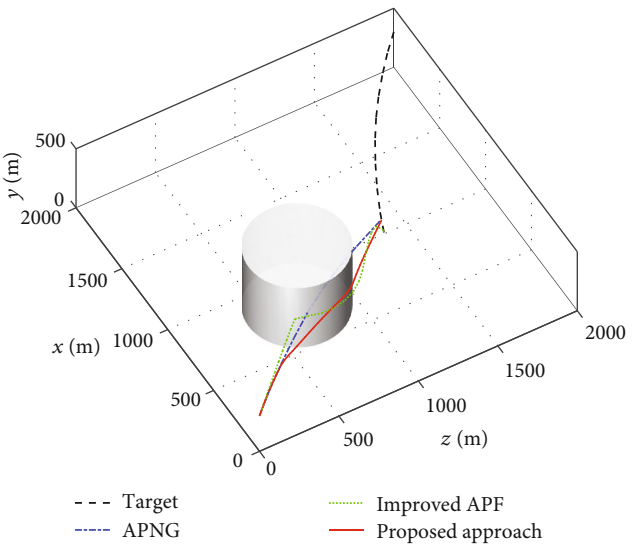

Figure 8: Flight trajectories of interceptor and target in case 1.

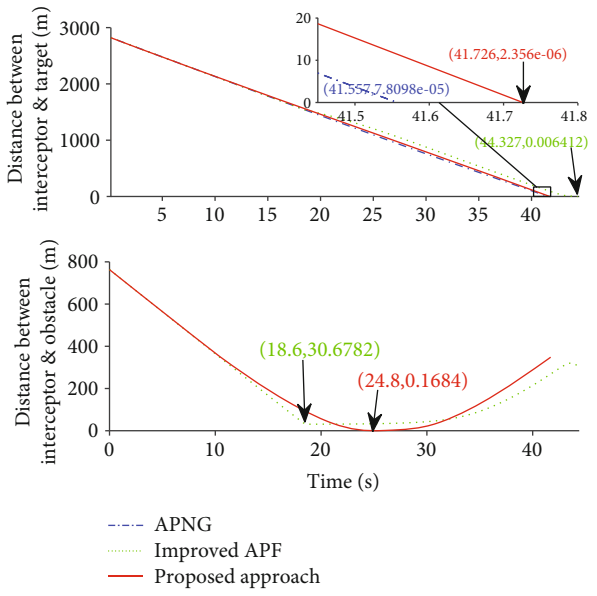

Figure 9: Changes of two distances in case 1.

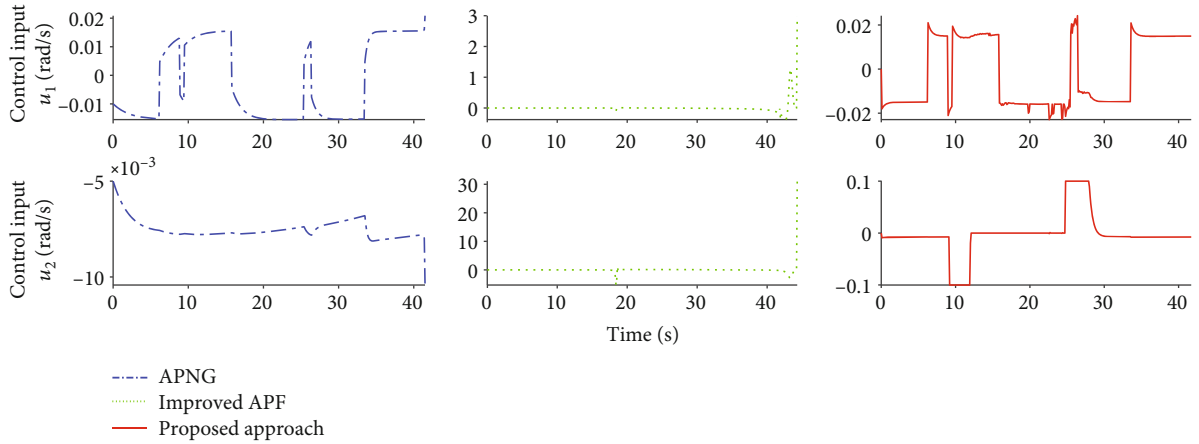

Figure 10: Changes of control inputs in case 1.

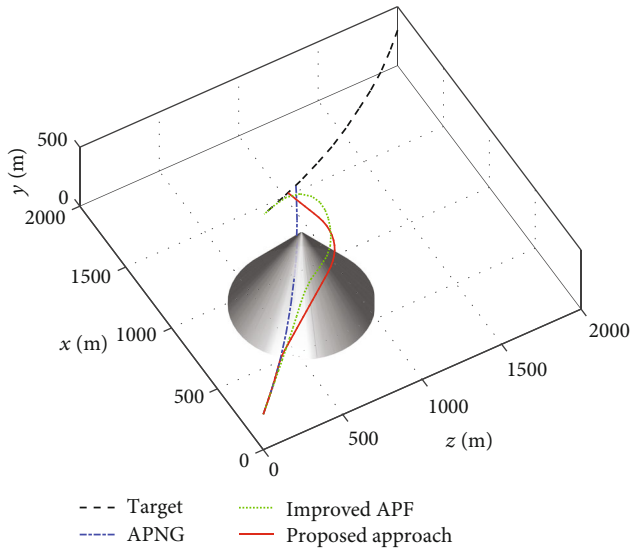

Figure 11: Flight trajectories of interceptor and target in case 2.

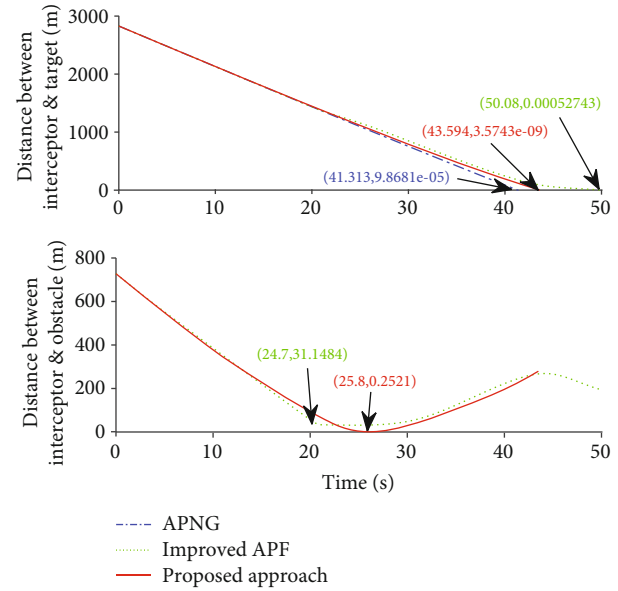

Figure 12: Changes of two distances in case 2.

According to Assumption (13), the estimation error meets

$$|\tilde{\varepsilon}_i(t)| \le \left\| \left[1, t, \cdots, t^{n-1}\right] \cdot \boldsymbol{\Gamma}_i^{-}(\boldsymbol{\Gamma}_i\boldsymbol{\Gamma}_i^{-} - \boldsymbol{I})^{-1}\boldsymbol{\varepsilon}_i \right\| + d_{\text{in}}\frac{|t|^n}{n!} \triangleq \bar{\varepsilon}_i(t). \tag{45}$$

From (45), we get the upper bound of the estimation error, which is only determined by the sampling instants and fitting errors. This conclusion will help to determine whether function $g_i(\boldsymbol{\alpha}_i^*, \cdot)$ could be used for extrapolation or not. Based on the above derivation, the implementation of the proposed estimation method is specified as follows:

Step 1. Before the start of guidance, we set the length of historical data as q, the allowance error of estimation as $\bar{\varepsilon}_{\text{allow}\,i}(t)$.

Step 2. At instant k, select k as zero moment, then the sampling instants prior to k can be noted as $t_j = -j\delta$ and $j = 1, \cdots, q$. Using historical data $(t_j, e_i(k-j))$ and $j = 1, \cdots, q$, we can get the coefficients $\boldsymbol{\alpha}_i^*(k) = [\alpha_{i0}^*(k), \cdots, \alpha_{i,n-1}^*(k)]^{\mathrm{T}}$ with Equation (39) and fitting error $\boldsymbol{\varepsilon}_i(k)$ with Equation (41). Then, with (45), we obtain the upper bound of the estimation error at $t_l = l\delta$ and $l = 0, \cdots, P-1$, which can be noted as $\bar{\varepsilon}_i(t_l)$.

Step 3. Compare $\bar{\varepsilon}_i(t_l)$ with $\bar{\varepsilon}_{\text{allow}\,i}(t)$, if $\bar{\varepsilon}_i(t_l) < \bar{\varepsilon}_{\text{allow}\,i}(t_l)$ for $\forall l = 0, \cdots, P-1$, indicating that we can use $g_i(\boldsymbol{\alpha}_i^*, \cdot)$ to estimate $e_i(k+l)$ without causing an error, then the estimation results shown in Equation (46) will be used for the feedforward compensation of the MPC controller.

$$\tilde{e}_i(k+l|k) = \left[1, t_l, \cdots, t_l^{n-1}\right] \cdot \boldsymbol{\alpha}_i^*(k), l = 0, \cdots, P-1. \tag{46}$$

Otherwise, if there exist $l = 0, \cdots, P-1$ that makes $\bar{\varepsilon}_i(t_l) > \bar{\varepsilon}_{\text{allow}\,i}(t_l)$, which indicates that a large error will be brought if we use $g_i(\boldsymbol{\alpha}_i^*, \cdot)$ to estimate $e_i(k+l)$, then, in order to avoid larger estimation error, we adopt the assumption that the disturbance remains unchanged in

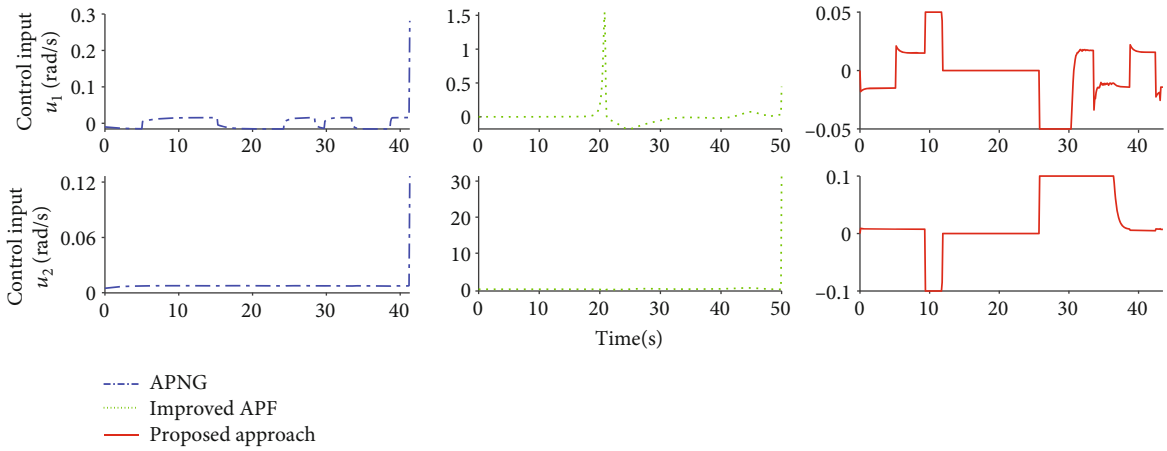

Figure 13: Changes of control inputs in case 2.

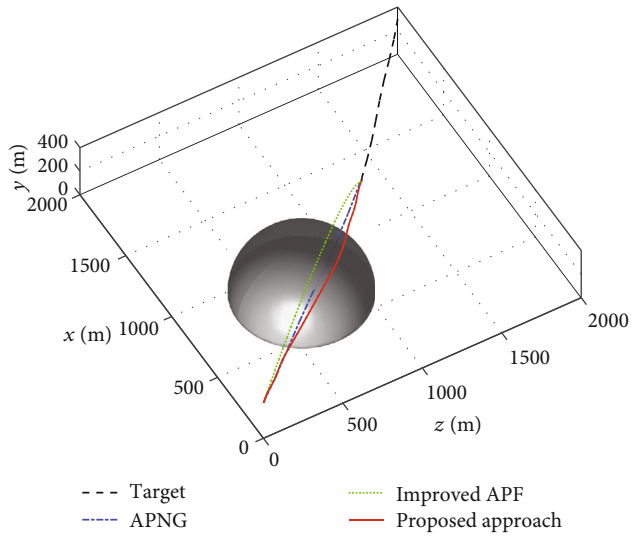

Figure 14: Flight trajectories of interceptor and target in case 3.

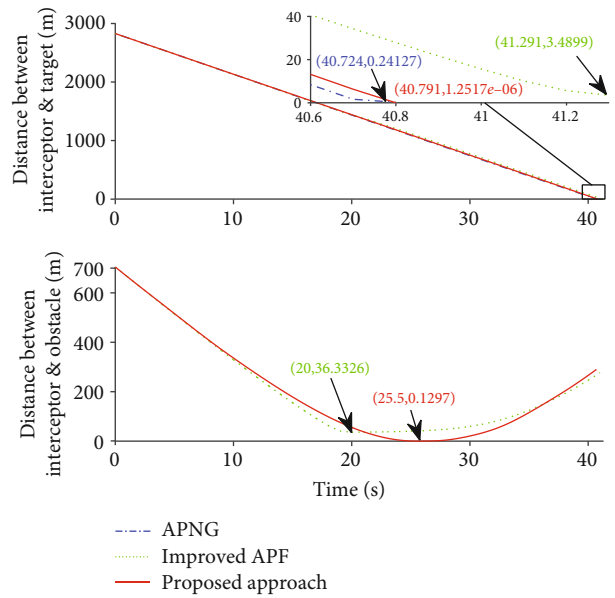

Figure 15: Changes of two distances in case 3.

the prediction horizon [36], that is

$$\tilde{e}_i(k+l|k) = e_i(k-1) + \Delta e_i(k-2) = 2e_i(k-1) - e_i(k-2), l = 0, \cdots, P-1. \quad (47)$$

Step 4. When the time comes $k+1$, the newest data $e_i(k)$ is obtained. Then, we let $k = k+1$and repeat step 2 and step 3.

In this way, we get $\tilde{\boldsymbol{e}}(k+l|k) = [\tilde{e}_1(k+l|k), \tilde{e}_2(k+l|k)]^{\mathrm{T}}$, $l = 0, \cdots, P-1$ at each instant k. Replacing the actual disturbances with the estimated ones, we can obtain the predicted system states as shown in Equation (48), instead of Equation (20).

$$\tilde{\boldsymbol{\chi}}(k+l|k) = \boldsymbol{F}(\tilde{\boldsymbol{\chi}}(k+l-1|k), \boldsymbol{u}(k+l-1), \tilde{\boldsymbol{e}}(k+l-1|k)), \quad (48)$$

where$\tilde{\boldsymbol{\chi}}(k|k) = \boldsymbol{\chi}(k)$.

Accordingly, the FHOCP Problem 7 can be rewritten as follows:

Problem 12. Given the system states $\boldsymbol{\chi}(k)$ and estimated value $\tilde{\boldsymbol{e}}(P;k)$, find the optimal control input sequence

$$\boldsymbol{u}^*(P;k) = \arg\min_{\boldsymbol{u}(P;k)} J_1(k, \tilde{\boldsymbol{\chi}}(P;k), \boldsymbol{u}(P;k), \tilde{\boldsymbol{e}}(P;k)), \quad (49)$$

subject to (22) and (48).

Now, we have finished the design of the MPC controller, the next work will be solving Problem 12 to obtain $\boldsymbol{u}^*(k)$. However, with the existence of complex constraints (48) and objective function (32), we can hardly get the analytical solution to Problem 12, thus a numerical

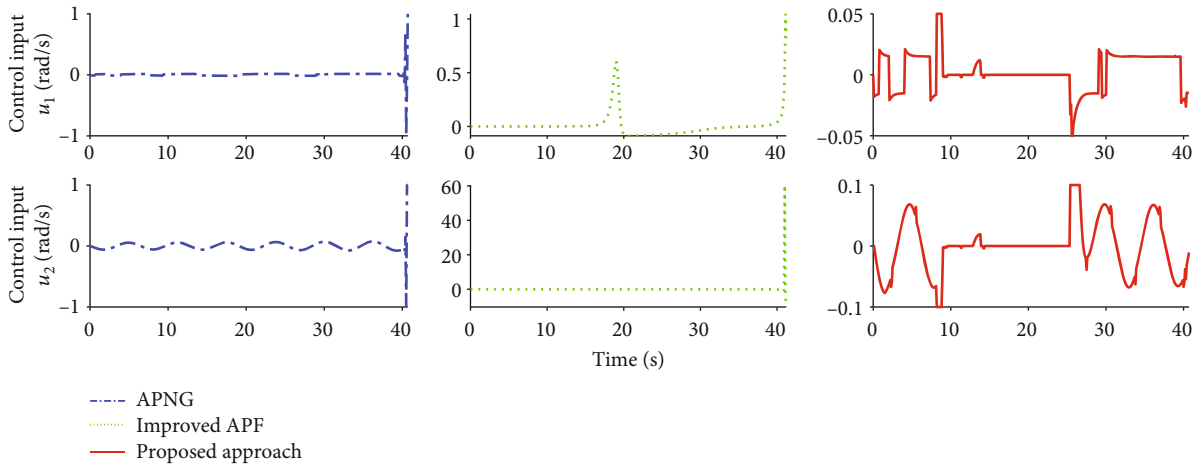

Figure 16: Changes of control inputs in case 3.

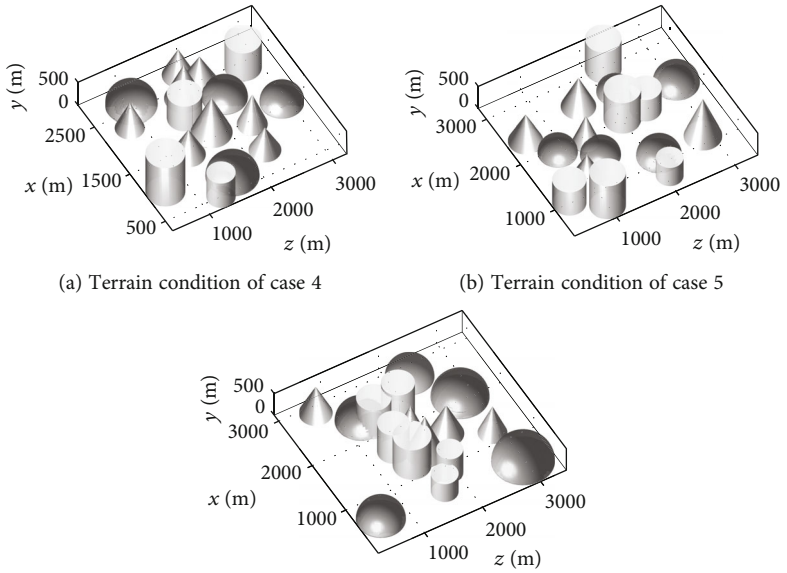

(a) Terrain condition of case 4

(b) Terrain condition of case 5

(c) Terrain condition of case 6

Figure 17: Terrain conditions of case 4, case 5, and case 6.

iterative method is needed. Aiming at improving the solving efficiency, we develop a hybrid solver for Problem 12 and Problem 14 (to be designed in Section 4) based on the adaptive moment estimation (Adam) algorithm, the solution procedure will be detailed in Section 4.3.

4. Guidance-Obstacle Avoidance Approach

After getting the optimal guidance command $\boldsymbol{u}^*(k)$ from the MPC controller, we should further consider whether taking $\boldsymbol{u}^*(k)$ as the actual input can guarantee the flight safety of the interceptor, and if not, how to successfully avoid the obstacles without affecting the guidance accuracy. To tackle the above issue, our main work in this section is as follows:

(1) Inspired by the velocity-obstacle model, we design a function to assess the threat from obstacles of different shapes, which is called the threat function

(2) By listing all possible situations related to the threat function, we derive the analytical expression of it and redefine Problem 6 as Problem 14

(3) Based on the Adam algorithm, we develop a hybrid solver for Problem 12 and Problem 14, whose output will serve as the real-time guidance command $\tilde{\boldsymbol{u}}^*(k)$ of the interceptor

4.1. Threat Assessment for a Single Obstacle Based on the Velocity-Obstacle Model. As a classical geometry-based method, VO has been proven to be effective when handling cases where obstacles are in the 2D form [29]. Its basic

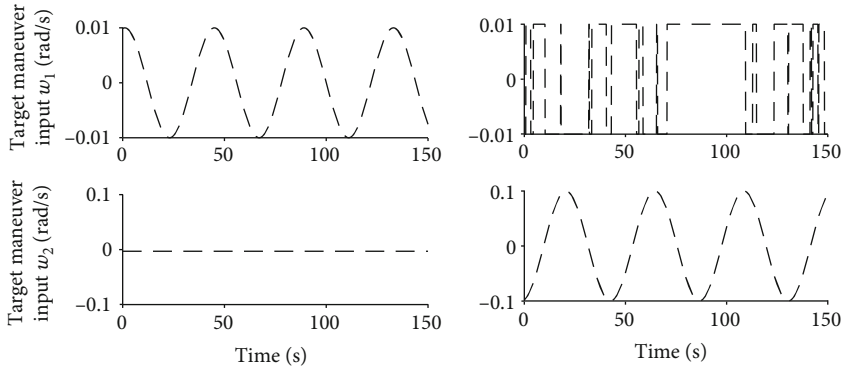

(a) Target maneuver input of case 4

(b) Target maneuver input of case 5

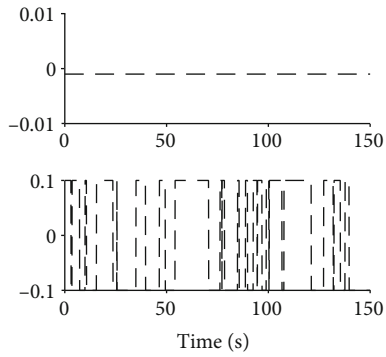

(c) Target maneuver input of case 6

Figure 18: Target maneuver inputs in case 4, case 5, and case 6.

principle is to find a set of flight angles, i.e., the collision cone. Along these angles, the interceptor will collide with obstacles. Nevertheless, when dealing with 3D obstacles of different shapes, it is rather difficult for VO to determine the boundary of the collision cone and establish its unified expression. Inspired by the VO model, we consider the relative motion of the interceptor and the obstacle and establish a unified function to assess the threat from obstacles of different shapes. Any feasible flight angle will be assigned a function value that depends on whether the interceptor will collide with the obstacle and, if so, the severity of the collision.

Considering the motion of the interceptor in the inertial coordinate system, if the interceptor makes no further maneuver, the change toΓ_i, according to (7), as shown in

$$\widetilde{\Gamma}_i(\boldsymbol{\chi}, \boldsymbol{\omega}_i, t) = (\chi_1 + \dot{\chi}_1 t - x_{oi})^2 + (\chi_3 + \dot{\chi}_3 t - z_{oi})^2 - \varsigma(\boldsymbol{\omega}_i, \chi_2 + \dot{\chi}_2 t). \tag{50}$$

Herein, the feasible range of t is

$$t \in \mathscr{T}_i = \left\{\tau \middle| 0 < \chi_2 + \dot{\chi}_2 \tau \le H_i \wedge \tau < t_{go}(\boldsymbol{\chi}) \wedge \tau > 0\right\}. \tag{51}$$

Remark 13. It can be noted from (51) that besides the existing constraint that limits the flight height of the interceptor to the range where the interceptor will probably collide with the obstacle, an additional constraint $t < t_{go}(\boldsymbol{\chi})$ is also put onto t, which is added for the case where the interceptor hits the target earlier than it encounters the obstacle.

Then, let

$$\lambda_i = \begin{cases} \lambda_{i1} = \dot{\chi}_1^{\,2} + \dot{\chi}_3^{\,2} - \omega_{i1}\dot{\chi}_2^{\,2}, \\ \lambda_{i2} = 2\dot{\chi}_1(\chi_1 - x_{oi}) + 2\dot{\chi}_3(\chi_3 - z_{oi}) - 2\omega_{i1}\chi_2\dot{\chi}_2 - \omega_{i2}\dot{\chi}_2, \\ \lambda_{i3} = (\chi_1 - x_{oi})^2 + (\chi_3 - z_{oi})^2 - \omega_{i1}\chi_2^{\,2} - \omega_{i2}\chi_2 - \omega_{i3}, \end{cases} \tag{52}$$

yielding

$$\widetilde{\Gamma}_i(\boldsymbol{\chi}, \boldsymbol{\omega}_i, t) = \lambda_{i1} t^2 + \lambda_{i2} t + \lambda_{i3}. \tag{53}$$

Define the threat function of the single obstacle as

$$\zeta_i(\boldsymbol{\chi}, \boldsymbol{\omega}_i) = \max\left(0, -\min_{t \in \mathscr{T}_i} \widetilde{\Gamma}_i(\boldsymbol{\chi}, \boldsymbol{\omega}_i, t)\right). \tag{54}$$

In this way, the deeper the interceptor enters the obstacle along its current heading, the greater the threat of the obstacle will be. If the interceptor does not collide with the obstacle without any further maneuvering, the threat of the

obstacle will be zero. However, since the feasible range of t involves different situations, the value of $\min_{t\in\mathscr{T}_i}\widetilde{\Gamma}_i(\boldsymbol{\chi},\boldsymbol{\omega}_i,t)$ in Equation (54) is hard to determine, hence around which further discussion is carried out.

4.2. Analytical Expression for Threat Function and Cost Function. In order to obtain the exact value of $\min_{t\in\mathscr{T}_i}\widetilde{\Gamma}_i(\boldsymbol{\chi},\boldsymbol{\omega}_i,t)$, all the possible situations related to $\mathscr{T}_i$ are summed up. From Equation (51), they are

$$\mathscr{T}_i=[a_i,b_i]=\begin{cases}\left[0,\dfrac{H_i-\chi_2}{\dot{\chi}_2}\right], & \chi_2<H_i\wedge\dot{\chi}_2>0\wedge\dfrac{H_i-\chi_2}{\dot{\chi}_2}\le t_{\mathrm{go}}(\boldsymbol{\chi}),\\ \left[0,-\dfrac{\chi_2}{\dot{\chi}_2}\right], & \chi_2<H_i\wedge\dot{\chi}_2<0\wedge-\dfrac{\chi_2}{\dot{\chi}_2}\le t_{\mathrm{go}}(\boldsymbol{\chi}),\\ \left[0,t_{\mathrm{go}}(\boldsymbol{\chi})\right], & \left(\chi_2<H_i\wedge\dot{\chi}_2>0\wedge\dfrac{H_i-\chi_2}{\dot{\chi}_2}>t_{\mathrm{go}}(\boldsymbol{\chi})\right)\vee\left(\chi_2<H_i\wedge\dot{\chi}_2<0\wedge-\dfrac{\chi_2}{\dot{\chi}_2}>t_{\mathrm{go}}(\boldsymbol{\chi})\right)\vee(\chi_2<H_i\wedge\dot{\chi}_2=0),\\ \left[\dfrac{H_i-\chi_2}{\dot{\chi}_2},-\dfrac{\chi_2}{\dot{\chi}_2}\right], & \chi_2\ge H_i\wedge\dot{\chi}_2<0\wedge-\dfrac{\chi_2}{\dot{\chi}_2}\le t_{\mathrm{go}}(\boldsymbol{\chi}),\\ \left[\dfrac{H_i-\chi_2}{\dot{\chi}_2},t_{\mathrm{go}}(\boldsymbol{\chi})\right], & \chi_2\ge H_i\wedge\dot{\chi}_2<0\wedge\dfrac{H_i-\chi_2}{\dot{\chi}_2}<t_{\mathrm{go}}(\boldsymbol{\chi})<-\dfrac{\chi_2}{\dot{\chi}_2},\\ \varnothing, & \text{else}\end{cases}\tag{55}$$

Figure 4 gives a visual representation of the above situations.

Then, according to the relationship between the extreme point of the monadic quadratic function and the endpoints of the feasible interval $\mathscr{T}_i$, as shown in Figure 5, $\min_{t\in\mathscr{T}_i}\widetilde{\Gamma}_i(\boldsymbol{\chi},\boldsymbol{\omega}_i,t)$ can be formulated as (56) in piecewise form.

$$\min_{t\in[a_i,b_i]}\widetilde{\Gamma}_i(\boldsymbol{\chi},\boldsymbol{\omega}_i,t)=\begin{cases}\widetilde{\Gamma}_i(\boldsymbol{\chi},\boldsymbol{\omega}_i,a_i), & \left(\lambda_{i1}>0\wedge-\dfrac{\lambda_{i2}}{2\lambda_{i1}}\le a_i\right)\vee\left(\lambda_{i1}<0\wedge-\dfrac{\lambda_{i2}}{2\lambda_{i1}}>b_i\right)\vee\left(\lambda_{i1}<0\wedge a_i<-\dfrac{\lambda_{i2}}{2\lambda_{i1}}\le b_i\wedge a_i+b_i+\dfrac{\lambda_{i2}}{\lambda_{i1}}<0\right),\\ \widetilde{\Gamma}_i(\boldsymbol{\chi},\boldsymbol{\omega}_i,b_i), & \left(\lambda_{i1}>0\wedge-\dfrac{\lambda_{i2}}{2\lambda_{i1}}>b_i\right)\vee\left(\lambda_{i1}<0\wedge-\dfrac{\lambda_{i2}}{2\lambda_{i1}}\le a_i\right)\vee\left(\lambda_{i1}<0\wedge a_i<-\dfrac{\lambda_{i2}}{2\lambda_{i1}}\le b_i\wedge a_i+b_i+\dfrac{\lambda_{i2}}{\lambda_{i1}}\ge 0\right),\\ \widetilde{\Gamma}_i\left(\boldsymbol{\chi},\boldsymbol{\omega}_i,-\dfrac{\lambda_{i2}}{2\lambda_{i1}}\right), & \lambda_{i1}>0\wedge a_i<-\dfrac{\lambda_{i2}}{2\lambda_{i1}}\le b_i.\end{cases}\tag{56}$$

Let

$$\min_{\mathscr{T}_i=\varnothing}\widetilde{\Gamma}_i(\boldsymbol{\chi},\boldsymbol{\omega}_i,t)=M,\tag{57}$$

where $M\in\mathbb{R}^+$ is a large positive rational number. Then, the value of $\zeta_i(\boldsymbol{\chi},\boldsymbol{\omega}_i)$ in any possible situation can be determined with (55), (56), (57), and (54).

The total cost of obstacle avoidance is regarded as the sum of threats from all the detected obstacles, that is (58). Using the predicted system states at the next sampling time, the objective function for Problem 6 can be defined as

$$J_2(\boldsymbol{\chi})=\sum_i^{n_o}\zeta_i(\boldsymbol{\chi},\boldsymbol{\omega}_i),\tag{58}$$

$$\begin{aligned}\tilde{J}_2(\boldsymbol{\chi}(k),\tilde{\boldsymbol{u}}(k))&=\|\tilde{\boldsymbol{u}}(k)-\boldsymbol{u}^*(k)\|_p+J_2(\boldsymbol{\chi}(k),\tilde{\boldsymbol{u}}(k))\\&=\|\tilde{\boldsymbol{u}}(k)-\boldsymbol{u}^*(k)\|_p+\sum_i^{n_o}\zeta_i(\tilde{\boldsymbol{\chi}}(k+1|k),\boldsymbol{\omega}_i).\end{aligned}\tag{59}$$

Herein, $\tilde{\boldsymbol{\chi}}(k+1|k)$ is obtained from Equation (48). Function images of $\tilde{J}_2$ in different situations are shown in Figure 6.

Finally, the optimal Problem 6 can be rewritten as follows:

Problem 14. Given the system states $\boldsymbol{\chi}(k)$, estimated value $\tilde{\boldsymbol{e}}(k|k)$, and the guidance command $\boldsymbol{u}^*(k)$ obtained from

Table 3: The initial states of the interceptor and the target in example 2.

	x(m)	y(m)	z(m)	$\theta(\pi$ rad)	$\psi(\pi$ rad)	v(m/s)
Interceptor	0	300	0	0	-1/4	40
Target	5000	300	5000	0	3/4	30

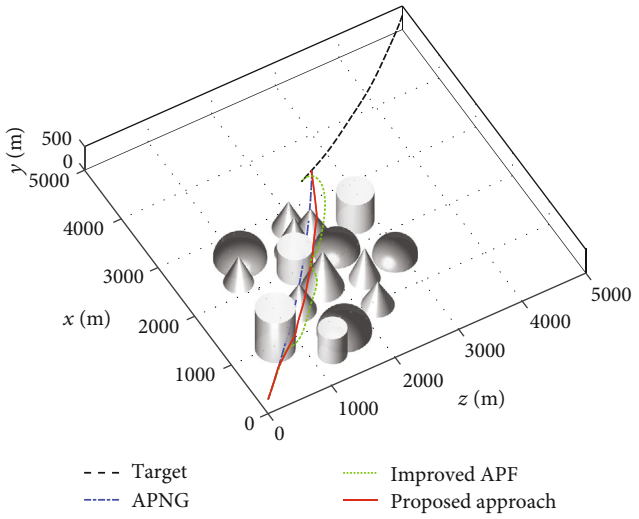

Figure 19: Flight trajectories of interceptor and target in case 4.

Problem 12, find the optimal guidance-obstacle avoidance command

$$\tilde{\boldsymbol{u}}^*(k) = \arg \min_{\tilde{\boldsymbol{u}}(k)} \tilde{J}_2(\boldsymbol{\chi}(k), \tilde{\boldsymbol{u}}(k)) = \arg \min_{\tilde{\boldsymbol{u}}(k)} \|\tilde{\boldsymbol{u}}(k) - \boldsymbol{u}^*(k)\|_p + \sum_i^{n_o} \zeta_i(\boldsymbol{F}(\boldsymbol{\chi}(k), \tilde{\boldsymbol{u}}(k), \tilde{\boldsymbol{e}}(k|k)), \boldsymbol{\omega}_i), \tag{60}$$

subject to

$$\tilde{\boldsymbol{u}}(k) \in \boldsymbol{\mathcal{U}}, \tag{61}$$

$$J_2(\boldsymbol{\chi}(k), \boldsymbol{u}^*(k)) > 0. \tag{62}$$

By solving Problem 14, we minimize the threat of obstacles while keeping the guidance command unchanged as much as possible, thus the guidance accuracy and the flight safety are both guaranteed. In the following part, we will elaborate on the solution process of Problem 12 and Problem 14.

4.3. Solver for the Optimal Guidance-Obstacle Avoidance Command. As an emerging algorithm in the deep learning field, Adam has great advantages in solving both convex and nonconvex optimization problems [37], it computes the adaptive learning rate for each optimization variable from estimates of the first and second moment of the gradient [38], thus improving the convergence speed of objective function in many optimization scenarios. However, affected by the initial solution, Adam is sometimes trapped in local optima like most single solution-based algorithms and requires further improvement in combination with specific situations.

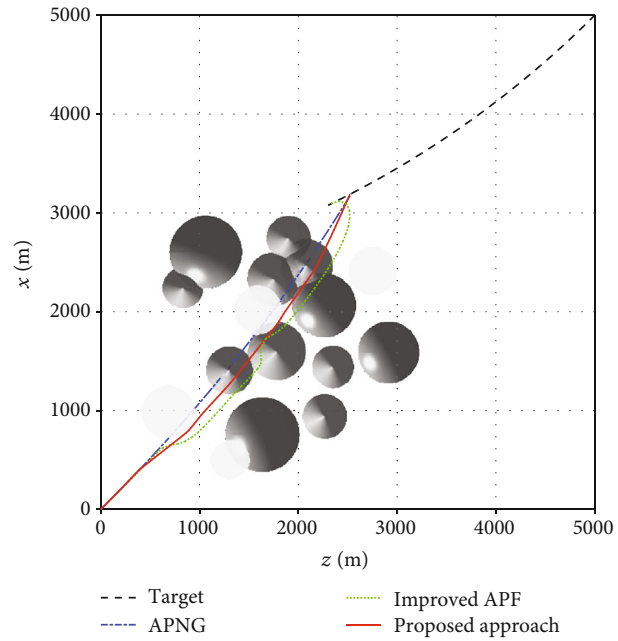

Figure 20: Flight trajectory projections of interceptor and target in case 4.

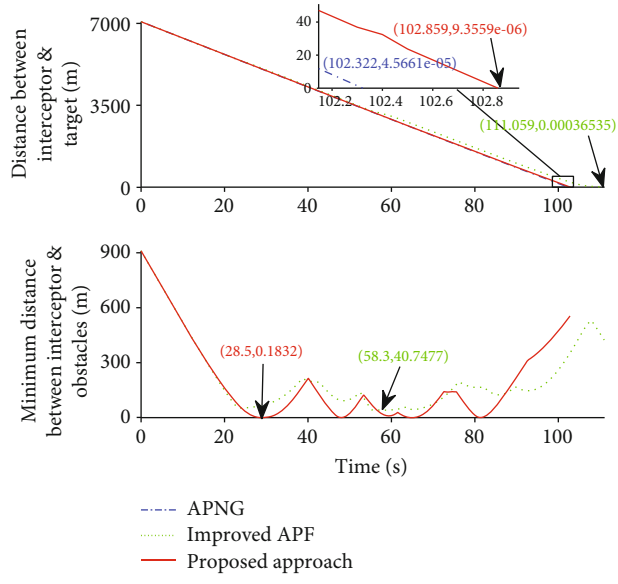

Figure 21: Changes of two distances in case 4.

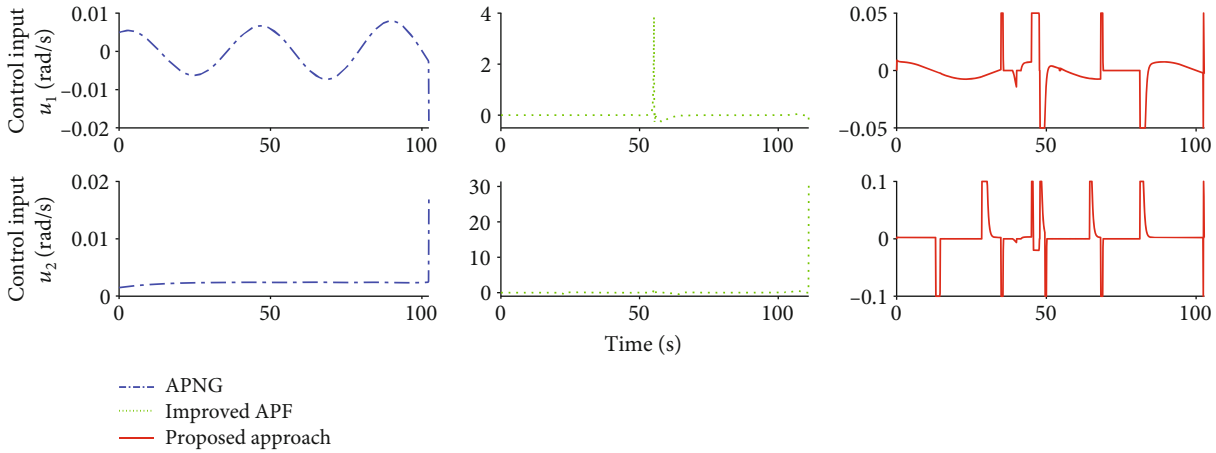

Figure 22: Changes of control inputs in case 4.

In this part, to get the optimal guidance-obstacle avoidance command while ensuring the real-time performance of control, the following arrangement is made:

(1) For high-dimensional optimal Problem 12 with a relatively simple objective function, the Adam based on single-point iteration is used for finding the optimal solution $\boldsymbol{u}^*(k)$. To guarantee the initial feasibility, we choose $\widehat{\boldsymbol{u}}(P;k)$ (which is constructed in Section 3.2) as the initial solution. That is

$$\boldsymbol{u}^{(0)}(P;k) = \widehat{\boldsymbol{u}}(P;k) \tag{63}$$

(2) For Problem 14 with a nonconvex objective function, the Adam is extended to a population-based algorithm. To expand the searching regions and help jump out of local optima, the opposition-based learning strategy is adopted when generating the initial population, which is to add the opposite individuals of selected ones into the initial population [39], in case the initial solutions may be far away from the optimal one

The initial solutions selected for Problem 14 are $\tilde{\boldsymbol{u}}^*(k-1)$, $\boldsymbol{u}^*(k)$, and $[0,0]^{\mathrm{T}}$, whose opposite individuals $-\tilde{\boldsymbol{u}}^*(k-1)$ and $-\boldsymbol{u}^*(k)$ will also be included in the initial population. Hence the initial population can be labeled as

$$\left\{\tilde{\boldsymbol{u}}_1^{(0)} = \tilde{\boldsymbol{u}}^*(k-1), \cdots, \tilde{\boldsymbol{u}}_5^{(0)} = -\boldsymbol{u}^*(k)\right\}. \tag{64}$$

The update rules for both $\boldsymbol{u}^{(iter)}(P;k)$ and $\tilde{\boldsymbol{u}}_j^{(iter)}$, $j = 1, \cdots, 5$ are identical, here to unified description, we denote $\boldsymbol{u}^{(iter)}(P;k)$, $\tilde{\boldsymbol{u}}_j^{(iter)}$ as $\boldsymbol{u}^{(iter)} \in \mathbb{R}^{Nu}$, and $J_1(\cdot)$, $\tilde{J}_2(\cdot)$ as $J(\boldsymbol{u}^{(iter)})$, so the update process of $\boldsymbol{u}^{(iter)}$ can be described as (65)–(70).

Get gradient with respect to the objective function

$$\boldsymbol{g}^{(\mathrm{iter})} = \nabla_{\boldsymbol{u}} J\left(\boldsymbol{u}^{(\mathrm{iter\text{-}1})}\right). \tag{65}$$

Update the biased first-moment estimate

$$\boldsymbol{\eta}^{(\mathrm{iter})} = \beta_1 \boldsymbol{\eta}^{(\mathrm{iter\text{-}1})} + (1-\beta_1)\boldsymbol{g}^{(\mathrm{iter})}. \tag{66}$$

Update the biased second-moment estimate

$$\boldsymbol{v}^{(\mathrm{iter})} = \beta_2 \boldsymbol{v}^{(\mathrm{iter\text{-}1})} + (1-\beta_2)\boldsymbol{g}^{(\mathrm{iter})} \odot \boldsymbol{g}^{(\mathrm{iter})}. \tag{67}$$

Compute the bias-corrected first-moment estimate

$$\widehat{\boldsymbol{\eta}}^{(\mathrm{iter})} = \boldsymbol{\eta}^{(\mathrm{iter})} / \left(1-\beta_1^{\mathrm{iter}}\right). \tag{68}$$

Compute bias-corrected second-moment estimate

$$\widehat{\boldsymbol{v}}^{(\mathrm{iter})} = \boldsymbol{v}^{(\mathrm{iter})} / \left(1-\beta_2^{iter}\right). \tag{69}$$

Update $\boldsymbol{u}^{(\mathrm{iter})}$

$$\boldsymbol{u}^{(\mathrm{iter})} = \boldsymbol{u}^{(\mathrm{iter\text{-}1})} - \alpha \cdot \widehat{\boldsymbol{\eta}}^{(\mathrm{iter})} / \left(\sqrt{\widehat{\boldsymbol{v}}^{(\mathrm{iter})}} + \varepsilon\right). \tag{70}$$

Herein, all operations on vectors are element-wise, β_1 and $\beta_2 \in (0,1]$ are the decay rates for the moment estimates, $\alpha \in (0,1]$ is the step size, and $\varepsilon \in \mathbb{R}^+$ is a small positive rational number. The initial biased moment estimates meet $\boldsymbol{\eta}^{(0)} = \boldsymbol{v}^{(0)} = \vartheta$.

Moreover, to make $\boldsymbol{u}^{(iter)} = [u_1^{(iter)}, \cdots, u_{Nu}^{(iter)}]^{\mathrm{T}}$ meet the control input constraints during iteration, the nonlinear

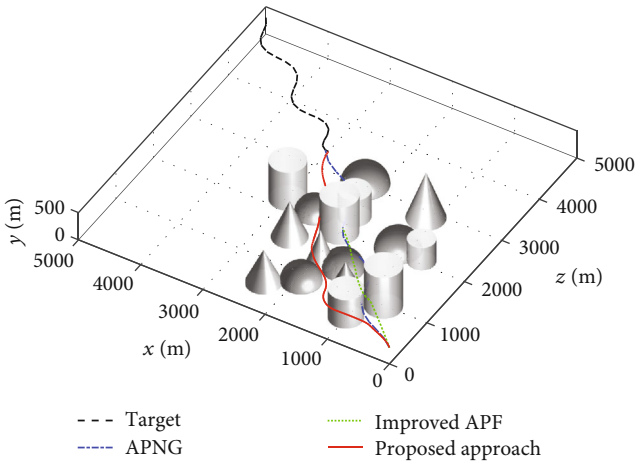

Figure 23: Flight trajectories of interceptor and target in case 5.

saturation function Sat(•) is introduced.

$$\mathrm{Sat}\left(u_i^{(\mathrm{iter})} \middle| U_{\max\, i}\right) = \begin{cases} u_i^{(\mathrm{iter})}, & \left|u_i^{(\mathrm{iter})}\right| \le U_{\max\, i}, \\ U_{\max\, i} \cdot \mathrm{sign}\left(u_i^{(iter)}\right), & \text{else.} \end{cases} \tag{71}$$

Then, $\boldsymbol{u}^{(\mathrm{iter})}$ will be corrected as shown in

$$\boldsymbol{u}^{(\mathrm{iter})} = \left[\mathrm{Sat}\left(u_1^{(\mathrm{iter})} \middle| U_{\max\, 1}\right), \cdots, \mathrm{Sat}\left(u_{Nu}^{(\mathrm{iter})} \middle| U_{\max\, Nu}\right)\right]^{\mathrm{T}}. \tag{72}$$

The stop criteria of iteration are formulated according to the number of invalid iterations and total iterations. Invalid iterations refer to those where the values of the objective function do not decrease significantly, so the number of invalid iterations can be expressed as

$$\kappa = \sum_{i=1}^{\mathrm{iter}} \sigma\left(J\left(\boldsymbol{u}^{(i)}\right) - J\left(\boldsymbol{u}^{(i-1)}\right) + \varepsilon_0\right), \tag{73}$$

where $\varepsilon_0 \in \mathbb{R}^+$ is a small positive rational number, $\sigma(\bullet)$ is the unit step function.

$$\sigma(J) = \begin{cases} 1, & J \ge 0, \\ 0, & J < 0, \end{cases} \tag{74}$$

The iteration will continue until there is

$$\kappa \ge \bar{K} \vee \mathrm{iter} \ge K. \tag{75}$$

So the optimal solution of Adam based on single point iteration can be determined as (76), or if the Adam is population-based, the optimal solution will be determined after

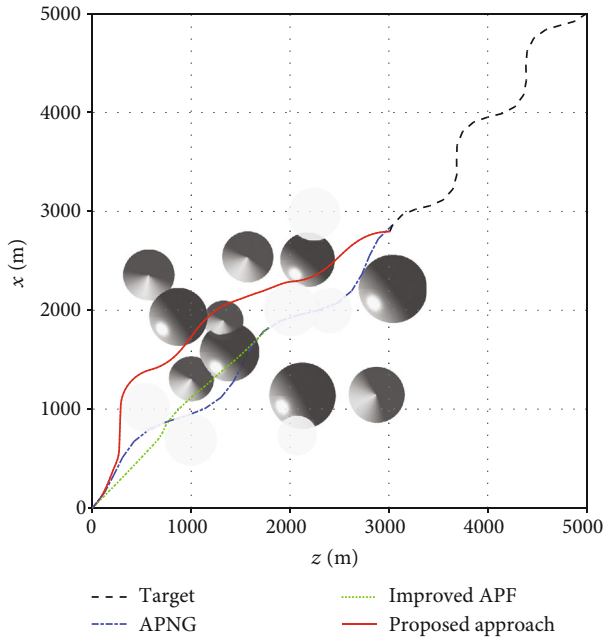

Figure 24: Flight trajectory projections of interceptor and target in case 5.

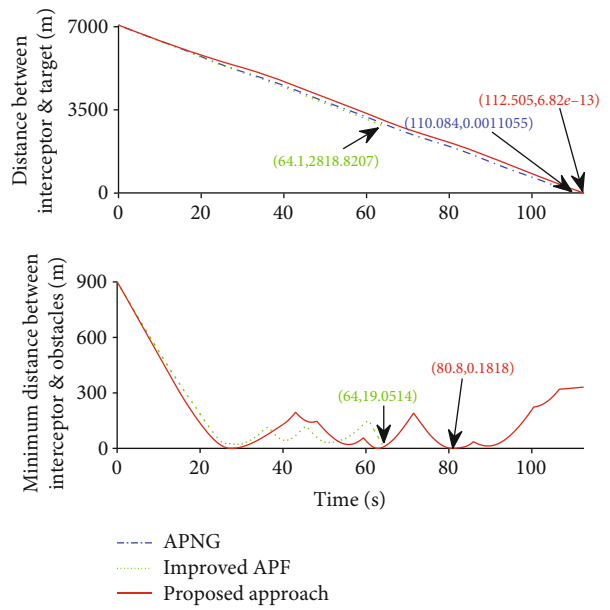

Figure 25: Changes of two distances in case 5.

iterations of all individuals are completed, that is

$$\boldsymbol{u}^* = \arg\min_{\boldsymbol{u}^{(i)}} J\left(\boldsymbol{u}^{(i)}\right), i = 0, \cdots, iter \tag{76}$$

$$\tilde{\boldsymbol{u}}^* = \arg\min_{\tilde{\boldsymbol{u}}_j^*} J\left(\tilde{\boldsymbol{u}}_j^*\right), j = 0, \cdots, N_{\mathrm{P}} \tag{77}$$

wherein $\tilde{\boldsymbol{u}}_j^*$ is the optimal individual and N_{P} is the population size.

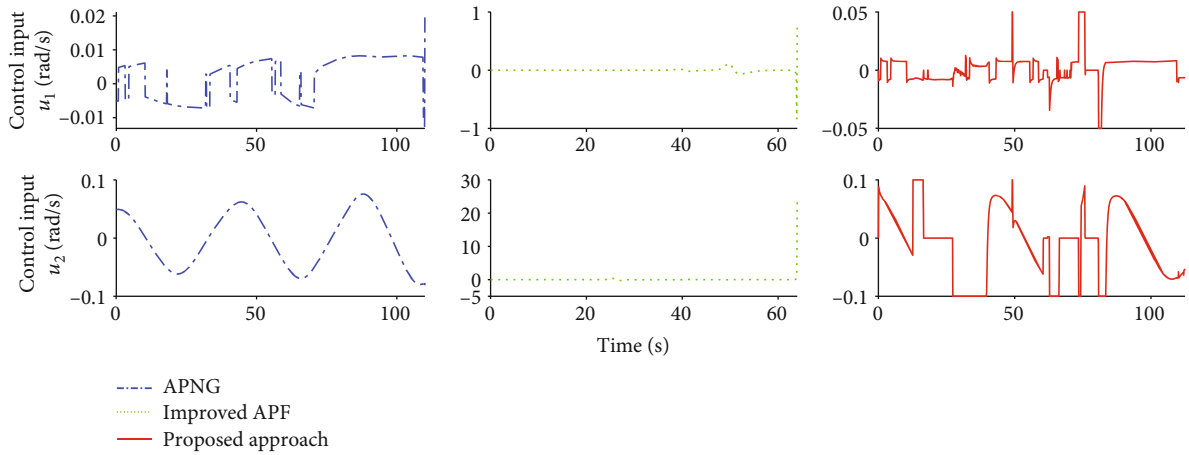

Figure 26: Changes of control inputs in case 5.

The complete pseudocode of the proposed hybrid solver for Problem 12 and Problem 14 is listed in Algorithm 1.

Now, we have finished the design of the proposed guidance approach with obstacle avoidance, whose complete implementation at each sampling instant is shown in Figure 7.

5. Numerical Simulation

In order to demonstrate the effectiveness of the proposed guidance-obstacle avoidance approach, simulations are performed in the single-obstacle scenario and multiobstacle scenario, respectively. Target maneuver inputs in both scenarios are randomly generated based on some common input signals, such as sine wave and random square wave. The simulation results of the proposed approach will be compared with those of the improved APF method [24] and APNG [6] in terms of guidance performance, obstacle avoidance performance, and maximum control inputs required. A Monte Carlo experiment is also performed to further demonstrate the robustness and computation efficiency of the approach.

5.1. Example 1 (Single-Obstacle Scenario). In this part, the interceptor will encounter one of the three typical obstacles in each case, to test the performance of the proposed approach in dealing with simple scenarios. The shape and position of the obstacle for each case are shown in Table 1.

The initial states of the interceptor and the target in three cases are shown in Table 2.

In all three cases, the sampling period and the length of the prediction horizon are set as Equation (78) and Equation (79), thus we can obtain the actual terminal miss distance according to Remark 9. The control input constraints for the proposed approach are set to $U_{\max 1} = 0.05$ rad/s and $U_{\max 2} = 0.1$ rad/s. The detection range of interceptor to obstacles, also known as the range of repulsive force in the APF method, is set to 400 m, and the scale factors of APNG are set to $k_1 = 10$ and $k_2 = 10$.

$$\delta = \begin{cases} 0.1, & t_{go} \geq \delta, \\ t_{go}, & \text{else}, \end{cases} \tag{78}$$

$$P = \begin{cases} 5, & t_{go} > \delta \cdot P_0, \\ 1, & \text{else}. \end{cases} \tag{79}$$

Simulation results of each case are shown in Figures 8–16, respectively. Wherein, Figures 8, 11, and 14 show the flight trajectories of the interceptor and target, it can be found that the interceptor using the proposed guidance-obstacle avoidance approach has a smoother trajectory than that using the improved APF method and needs fewer corrective maneuver actions in the endgame of guidance. Figures 9, 12, and 15 represent the change in distance between the interceptor and target, as well as the change in distance between the interceptor and obstacle. It can be noticed that, in terms of guidance performance, the proposed approach achieves the highest guidance accuracy in all three cases, followed by APNG. The improved APF method ranks last, still, its guidance accuracy is acceptable, which is because the interceptor using the APF method makes large-amplitude maneuver actions in the endgame of guidance to pursue the target, as shown in Figures 10, 13, and 16. However, for most interceptors with limited maneuverability, it is impractical to conduct such a maneuver that the instant angular velocity is up to 60 rad/s (which represents an overload of up to 240 g under the given velocity), so the guidance accuracy of the improved APF method in practice may be much lower than that in the simulation. The interceptor using the proposed approach, by contrast, keeps its control inputs within limits all through the guidance process. In terms of obstacle avoidance performance, the interceptors using the proposed approach and using the improved APF method successfully avoid collision in all

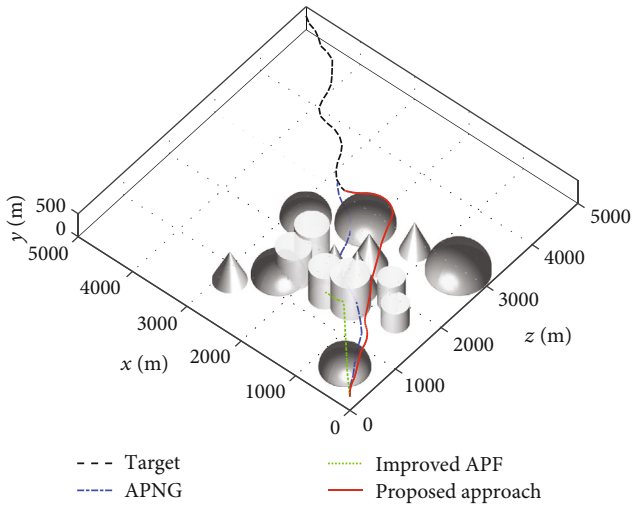

Figure 27: Flight trajectories of interceptor and target in case 6.

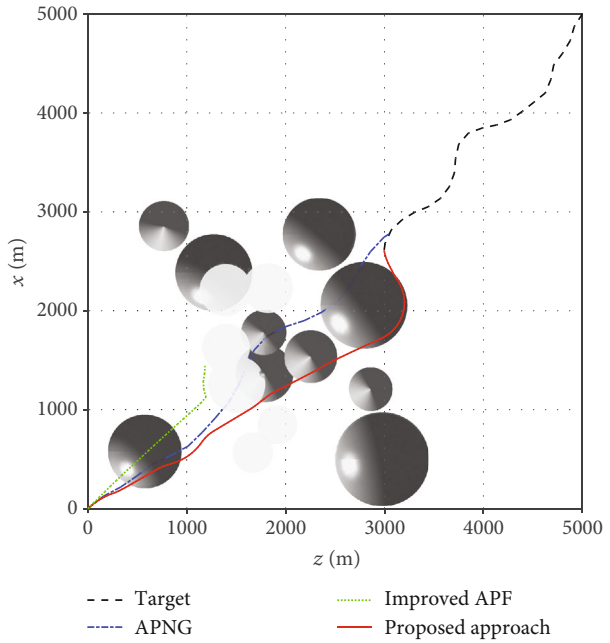

Figure 28: Flight trajectory projections of interceptor and target in case 6.

three cases; however, under the same set of detection range, the interceptor using the proposed approach performs evasive maneuver earlier than that using APF and requires smaller control inputs.

5.2. Example 2 (Multiobstacle Scenario). In this part, the random terrain with multiple obstacles is created for each case (case 4, case 5, and case 6), and the proposed approach will be tested whether it can adapt to more complicated situations. The terrain and the target maneuver input in each case are shown in Figures 17 and 18. The initial states of the interceptor and the target in three cases can be seen in Table 3, and other simulation parameters are the same as those in example 1. Similarly, the maximum control inputs are still used for comparison together with the guidance accuracy and obstacle avoidance performance.

Simulation results of each case are shown in Figures 19–30, respectively. Wherein Figures 19, 23, and 27 show the flight trajectories of the interceptor and the target in 3D space, whose projections on the plane *zOx* are shown in Figures 20, 24, and 28. Figures 21, 25, and 29 represent the change in distance between the interceptor and the target, as well as the change in minimum distance between the interceptor and obstacles. Figures 22, 26, and 30 show the change of control inputs for different methods. It can be found that the interceptor using the improved APF method approaches the target faster in the initial phase, whereas interceptors using the proposed approach and APNG end up with a smaller miss distance. The principal reason is that the latter two methods focus more on the future motion of both sides, while the former only takes the current position of the target into account, thus making it unable to cope with the target maneuver in the endgame. It also can be noted that in case 5 and case 6, the improved APF method fails to escape the local optima when addressing overlapping obstacles, so the interceptor cannot further approach the target, while the interceptor

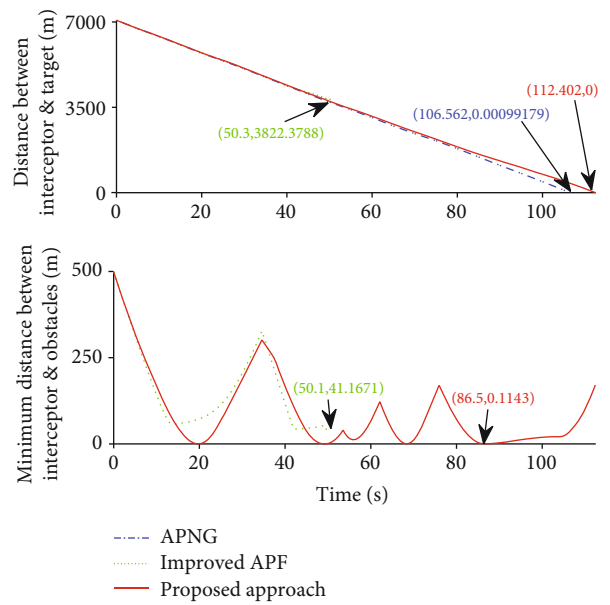

Figure 29: Changes of two distances in case 6.

using the proposed approach successfully avoids multiple overlapping obstacles and achieves the highest guidance accuracy in all three cases, which illustrates that the proposed approach is more robust when facing complicated situations. Moreover, with the proposed approach, the control inputs of the interceptor can always be limited to the given ranges, which provides the condition for applying the proposed approach to other types of interceptors.

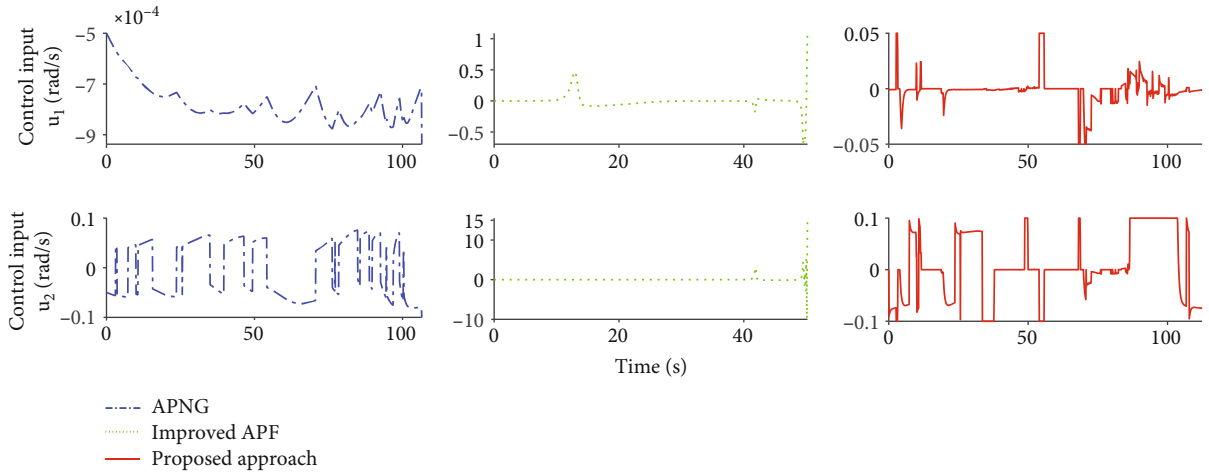

Figure 30: Changes of control inputs in case 6.

Table 4: The generation rules of the target maneuver input in Monte Carlo experiment.

Random number $\mu_{1i}\mu_{1i} \in [0,1]$, $i = 1,2$	Form of signal	Maneuver input $w_i(t)$ (μ_{2i}, t_{ji} are random numbers)
$\mu_{1i} \le 0.33$	Constant	$w_i(t) = (2\mu_{2i} - 1)w_{\max\ i}$, $\mu_{2i} \in [0,1]$
$0.33 < \mu_{1i} \le 0.67$	Sine wave	$w_i(t) = w_{\max\ i} \sin(\mu_{2i} t)$, $\mu_{2i} \in [0,1]$
$\mu_{1i} > 0.67$	Square wave	$w_i(t) = \begin{cases} w_{\max\ i}, & t \in [t_{2j,i}, t_{2j+1,i}), \\ -w_{\max\ i}, & t \in [t_{2j-1,i}, t_{2j,i}), \end{cases}$, $t_{1i} < t_{2i} < \cdots \in \mathbb{Q}^+$

5.3. Monte Carlo Experiment. In order to further demonstrate the robustness and computation efficiency of the proposed approach, a Monte Carlo experiment is performed. Under the terrain condition of case 5, the interceptor is required to intercept a target in each simulation, where the target maneuver input is generated based on some random signals (see Table 4 for the generation rules). The experiment is carried out with the hardware of an Intel (R) Core (TM) i7-10750H CPU at 2.60GHz, 2.59 GHz, and 16GB RAM, and the parameters of the hybrid solver are set to $\bar{K}_1 = 3$, $K_1 = 100$, $\bar{K}_2 = 5$, and$K_2 = 30$. The initial states of both sides and other simulation parameters are the same as those in example 2.

To make the results more representative, the cases where the interceptor does not need to avoid obstacles are excluded from the experiment. For each simulation, the terminal miss distance, the minimum distance between the interceptor and obstacles, and the average computation duration (at each sampling instant) are recorded. Finally, 100 groups of results will be retained.

Figures 31–33 show the results of each simulation. Figures 34–36 show the statistical distribution and cumulative frequency of the above three indexes. Wherein, the average terminal miss distance of all simulations is 1.7315×10^{-5} m, the total success rate of obstacle avoidance is 96%, and the average computation duration at each sampling instant is 0.0113 s. In terms of robustness, the proposed approach can achieve a high guidance accuracy against maneuvering targets and a satisfying obstacle avoidance success rate under

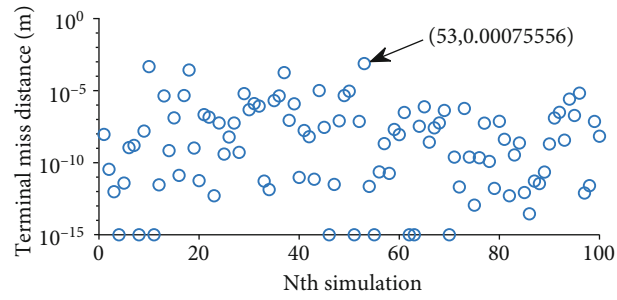

Figure 31: Terminal miss distance of each simulation.

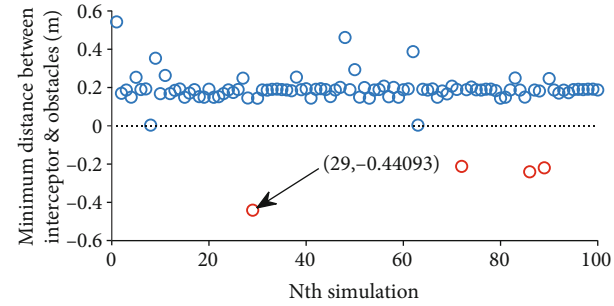

Figure 32: Minimum distance between the interceptor and obstacles of each simulation.

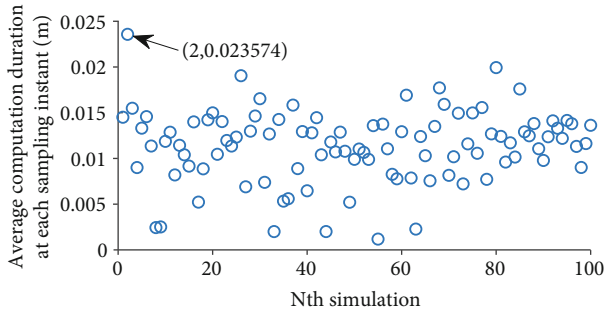

Figure 33: The average computation duration of each simulation.

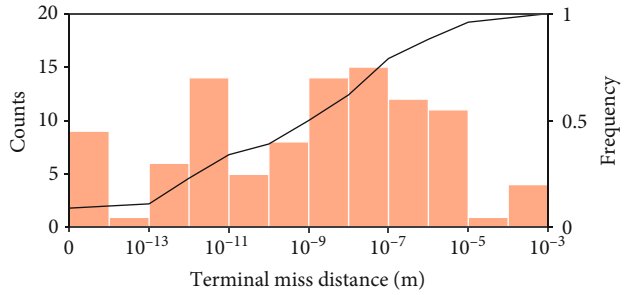

Figure 34: Statistical distribution and cumulative frequency of the terminal miss distance.

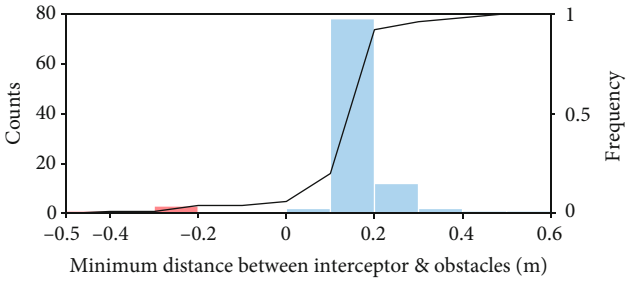

Figure 35: Statistical distribution and cumulative frequency of the minimum distance between the interceptor and obstacles.

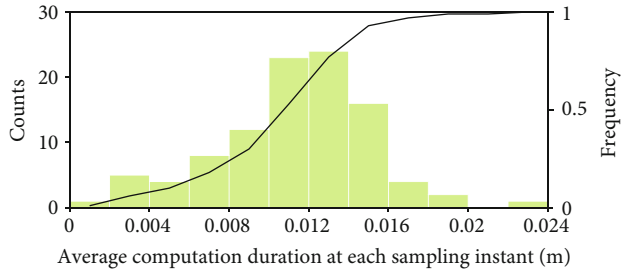

Figure 36: Statistical distribution and cumulative frequency of the average computation duration.

complicated terrain conditions. As for computation efficiency, the average computation duration of the approach is about one-tenth of the set sampling period, which means a relatively ample response time left for the control actuator of the interceptor.

From the results of the Monte Carlo experiment, the proposed approach can be extended to more application scenarios and has the opportunity to be further applied to engineering practice.

6. Conclusion

Three-dimensional guidance against maneuvering targets with requirements for obstacle avoidance is studied in this paper, and a novel guidance approach based on optimization techniques and MPC theory is proposed. Firstly, we decompose the optimal guidance problem into two-associated subproblems and provide the overall scheme of guidance on this basis. Secondly, the MPC controller with disturbance estimator is designed for the maneuvering target interception, thus we obtain a FHOCP in place of the optimization problem with uncertain terminal time. Then, to address the optimal guidance-obstacle avoidance problem, we design a unified function to assess the threat from obstacles of different shapes. Finally, a hybrid solver is developed to get the real-time guidance command. Numerical simulation and a Monte Carlo experiment are carried out to demonstrate the effectiveness and robustness of the proposed approach, and it is shown that, compared with some existing methods, the guidance approach presented in this paper has obvious advantages in both guidance and obstacle avoidance performance, even if the maneuverability of interceptor is limited. Our future work will focus on the cooperative guidance of multiple interceptors in a complex environment with threats and obstacles, the terminal impact angle will also be considered.

Appendix

Proof of Theorem 11. Apply $\boldsymbol{u}_\kappa$ to the system, then calculate the second derivative of $\boldsymbol{r}$ with respect to time, we can get

$$\begin{aligned}
\ddot{r}_x &= v_M(-u_{\kappa 1}\sin\chi_4\cos\chi_5 - u_{\kappa 2}\cos\chi_4\sin\chi_5) + \tilde{w}_x,\\
\ddot{r}_y &= v_M(u_{\kappa 1}\cos\chi_4) + \tilde{w}_y,\\
\ddot{r}_z &= v_M(u_{\kappa 1}\sin\chi_4\sin\chi_5 - u_{\kappa 2}\cos\chi_4\cos\chi_5) + \tilde{w}_y,
\end{aligned} \tag{A.1}$$

$$\begin{aligned}
r_x\ddot{r}_y - r_y\ddot{r}_x &= u_{\kappa 1}v_M(r_y\sin\chi_4\cos\chi_5 + r_x\cos\chi_4)\\
&\quad + u_{\kappa 2}v_M r_y\cos\chi_4\sin\chi_5 - r_y\tilde{w}_x + r_x\tilde{w}_y\\
&= \underbrace{u_{\kappa 1}\left[(r_x\dot{\chi}_3 - r_z\dot{\chi}_1)\sin\chi_5 + v_M(r_y\sin\chi_4\cos\chi_5 + r_x\cos\chi_4)\right]}_{\Xi}\\
&\quad + K_1\sin^2\chi_5 - K_2\sin\chi_5\cos\chi_5 - r_y\tilde{w}_x + r_x\tilde{w}_y.
\end{aligned} \tag{A.2}$$

According to (29), we have

$$\begin{aligned}\Xi &= \frac{(K_1\cos\chi_5 + K_2\sin\chi_5)\left[(r_x\dot{\chi}_3 - r_z\dot{\chi}_1)\sin\chi_5 + v_M(r_y\sin\chi_4\cos\chi_5 + r_x\cos\chi_4)\right]}{r_x\dot{\chi}_1 + r_y\dot{\chi}_2 + r_z\dot{\chi}_3} \\ &= \frac{K_1\left(-r_x\dot{\chi}_1\sin^2\chi_5 + r_z\dot{\chi}_3\cos^2\chi_5 + r_y\dot{\chi}_2\cos^2\chi_5 + r_x\dot{\chi}_1\right)}{r_x\dot{\chi}_1 + r_y\dot{\chi}_2 + r_z\dot{\chi}_3} + \frac{K_2\left(r_x\dot{\chi}_3\sin^2\chi_5 + r_z\dot{\chi}_3\cos\chi_5\sin\chi_5 + r_y\dot{\chi}_2\cos\chi_5\sin\chi_5 - r_x\dot{\chi}_3\right)}{r_x\dot{\chi}_1 + r_y\dot{\chi}_2 + r_z\dot{\chi}_3} \\ &= K_1\cos^2\chi_5 + K_2\cos\chi_5\sin\chi_5.\end{aligned} \tag{A.3}$$

Substituting (A.3) into (A.2), yields

$$r_x\ddot{r}_y - r_y\ddot{r}_x = K_1 - r_y\tilde{\omega}_x + r_x\tilde{\omega}_y = -\lambda\left(r_x\dot{r}_y - r_y\dot{r}_x\right). \tag{A.4}$$

Similarly, we can get

$$r_y\ddot{r}_z - r_z\ddot{r}_y = K_2 - r_y\tilde{\omega}_z + r_z\tilde{\omega}_y = -\lambda\left(r_y\dot{r}_z - r_z\dot{r}_y\right). \tag{A.5}$$

Simultaneous Equations (A.4) and (A.5), we obtain

$$r_x\ddot{r}_z - r_z\ddot{r}_x = -\lambda(r_x\dot{r}_z - r_z\dot{r}_x). \tag{A.6}$$

Also, according to (28), there are

$$\begin{aligned}\dot{J}_T &= 2\rho\left[\left(r_x\ddot{r}_y - r_y\ddot{r}_x\right)\left(r_x\dot{r}_y - r_y\dot{r}_x\right) + \left(r_y\ddot{r}_z - r_z\ddot{r}_y\right)\left(r_y\dot{r}_z - r_z\dot{r}_y\right)\right. \\ &\quad \left. + \left(r_x\ddot{r}_z - r_z\ddot{r}_x\right)\left(r_x\dot{r}_z - r_z\dot{r}_x\right)\right] = -2\lambda\rho\left[\left(r_x\dot{r}_y - r_y\dot{r}_x\right)^2\right. \\ &\quad \left. + \left(r_y\dot{r}_z - r_z\dot{r}_y\right)^2 + \left(r_x\dot{r}_z - r_z\dot{r}_x\right)^2\right] = -2\lambda\rho L,\end{aligned} \tag{A.7}$$

$$\dot{L} = -2\lambda L \le 0. \tag{A.8}$$

Then, calculate the integral of Equation (A.7) from k to $k+1$, we can get

$$J_T(k+1) - J_T(k) = \int_k^{k+1} J_T(\tau)\mathrm{d}\tau = \int_k^{k+1} -2\lambda\rho L(\tau)\mathrm{d}\tau \le -2\lambda\rho\delta L(k+1). \tag{A.9}$$

Applying

$$\lambda > \frac{1}{2(\rho-1)\delta}, \lambda \in \mathbb{R} \tag{A.10}$$

to (A.9), yields

$$\begin{aligned}J_T(k+1) - J_T(k) + L(k) &\le -\frac{\rho}{(\rho-1)}L(k+1) + L(k) \\ &= -\frac{\rho L(k+1) - \rho L(k) + L(k)}{(\rho-1)} = -\frac{J_T L(k+1) - J_T L(k) + L(k)}{(\rho-1)}.\end{aligned} \tag{A.11}$$

Therefore,

$$J_T(k+1) - J_T(k) + L(k) \le 0. \tag{A.12}$$

That is to say, for any $k > 0$, under the auxiliary controller (29), inequality (A.12) holds.

Then, considering the backward difference of the objective function at the instant k, it is

$$\begin{aligned}J_1(k) - J_1{}^*(k-1) &= J_T(k+P|k) - J_T(k+P-1|k-1) \\ &\quad + \sum_{l=0}^{P-1} L(\chi(k+l|k)) - \sum_{l=0}^{P-1} L(\chi^*(k+l-1|k-1))\end{aligned} \tag{A.13}$$

Apply $\hat{\boldsymbol{u}}(P;k)$ at the instant k. Because $\hat{\boldsymbol{u}}(k+l|k) = \boldsymbol{u}^*(k+l|k-1)$ and $l = 0, \cdots, P-2$, there are $L(\chi(k+l|k)) = L(\chi^*(k+l|k-1))$ and $J_T(k+P-1|k-1) = J_T(k+P-1|k)$, then Equation (A.13) is equal to

$$\begin{aligned}J_1(k) - J_1{}^*(k-1) &= J_T(k+P|k) - J_T(k+P-1|k) \\ &\quad + L(\chi(k+P-1|k)) - L(\chi^*(k-1|k-1)).\end{aligned} \tag{A.14}$$

Substituting (A.12) into (A.14), yields

$$J_1(k) - J_1{}^*(k-1) \le -L(\chi^*(k-1|k-1)). \tag{A.15}$$

Select Lyapunov function as $V(k) = J_1{}^*(k)$, then there is

$$V(k) - V(k-1) \le J_1(k) - J_1{}^*(k-1) \le -L(\chi^*(k-1|k-1)). \tag{A.16}$$

Therefore, the guidance system constructed on MPC is exponentially stable, and Theorem 11 holds. □

Data Availability

The data used to support the findings of this study are included within the article.

Conflicts of Interest

The authors declare that they have no conflicts of interest.

Acknowledgments

This research was funded by the Shandong Natural Science (ZR2020MF090).

References

[1] S. X. Liu, B. Yan, T. Zhang, X. Zhang, and J. Yan, "Three-dimensional coverage-based cooperative guidance law with overload constraints to intercept a hypersonic vehicle," *Aerospace Science and Technology*, vol. 130, article 107908, 2022.

[2] S. X. Liu, B. Yan, T. Zhang, X. Zhang, and J. Yan, "Coverage-based cooperative guidance law for intercepting hypersonic vehicles with overload constraint," *Aerospace Science and Technology*, vol. 126, article 107651, 2022.

[3] M. Guelman and J. Shinar, "Optimal guidance law in the plane," *Journal of Guidance, Control, and Dynamics*, vol. 7, no. 4, pp. 471–476, 1984.

[4] J. W. Song, Q. L. Xia, and J. X. Xu, "Modeling and analysis of guidance loop with velocity pursuit guidance law," *Acta Armamentarii*, vol. 29, no. 3, pp. 323–326, 2008.

[5] P. Zarchan, *Tactical and Strategic Missile Guidance, Sixth Edition*, American Institute of Aeronautics and Astronautics, Inc., Reston, Virginia, 2012.

[6] J. Shen, "Research on generalized guidance law of anti-tactical ballistic missiles," *Acta Armamentarii*, vol. 36, Supplement2, pp. 25–29, 2015.

[7] H. B. Ji, X. Liu, Z. Song, and Y. Zhao, "Time-varying sliding mode guidance scheme for maneuvering target interception with impact angle constraint," *Journal of the Franklin Institute*, vol. 355, no. 18, pp. 9192–9208, 2018.

[8] H. Gürsoy-Demir and M. Önder Efe, "A nonlinear disturbance observer-based adaptive integral sliding mode control for missile guidance system," *International Journal of General Systems*, vol. 51, no. 5, pp. 474–493, 2022.

[9] X. X. Wang, H. Q. Lu, X. L. Huang, Y. F. Yang, and Z. Y. Zuo, "Three-dimensional time-varying sliding mode guidance law against maneuvering targets with terminal angle constraint," *Chinese Journal of Aeronautics*, vol. 35, no. 4, pp. 303–319, 2022.

[10] C. M. Lin and C. F. Hsu, "Guidance law design by adaptive fuzzy sliding-mode control," *Journal of Guidance, Control, and Dynamics*, vol. 25, no. 2, pp. 248–256, 2002.

[11] D. Zhou, C. Mu, and W. Xu, "Adaptive sliding-mode guidance of a homing missile," *Journal of Guidance Control and Dynamics*, vol. 22, no. 4, pp. 589–594, 1999.

[12] B. Biswas, A. Maity, and S. R. Kumar, "Finite-time convergent three-dimensional nonlinear intercept angle guidance," *Journal of Guidance, Control, and Dynamics*, vol. 43, no. 1, pp. 146–153, 2020.

[13] Z. Chen, W. Chen, X. Liu, and J. Cheng, "Three-dimensional fixed-time robust cooperative guidance law for simultaneous attack with impact angle constraint," *Aerospace Science and Technology*, vol. 110, article 106523, 2021.

[14] I. Rusnak and L. Meir, "Optimal guidance for acceleration constrained missile and maneuvering target," *IEEE Transactions on Aerospace and Electronic Systems*, vol. 26, no. 4, pp. 618–624, 1990.

[15] Q. Zhang, Z. Wang, and F. Tao, "Optimal guidance law design for impact with terminal angle of attack constraint," *Optik*, vol. 125, no. 1, pp. 243–251, 2014.

[16] Y. W. Kim, B. Kim, C. H. Lee, and S. M. He, "A unified formulation of optimal guidance-to-collision law for accelerating and decelerating targets," *Chinese Journal of Aeronautics*, vol. 35, no. 7, pp. 40–54, 2022.

[17] M. Weiss and T. Shima, "Linear quadratic optimal control-based missile guidance law with obstacle avoidance," *IEEE Transactions on Aerospace and Electronic Systems*, vol. 55, no. 1, pp. 205–214, 2019.

[18] K. Shen, J. Wang, G. Li, J. Y. Shan, and I. R. Petersen, "Optimal cooperative guidance law for salvo attack: an MPC-based consensus perspective," *IEEE Transactions on Aerospace & Electronic Systems*, vol. 54, no. 5, pp. 2397–2410, 2018.

[19] J. Zhao, S. Zhou, and R. Zhou, "Distributed time-constrained guidance using nonlinear model predictive control," *Nonlinear Dynamics*, vol. 84, no. 3, pp. 1399–1416, 2016.

[20] S. C. Han and H. Bang, "Proportional navigation-based optimal collision avoidance for UAVs," *Journal of Institute of Control Robotics & Systems*, vol. 10, no. 11, pp. 1065–1070, 2004.

[21] L. I. Xia, J. H. Zhang, W. J. Xie, X. S. Li, and S. G. Zhong, "Research on autonomic collision avoidance method for UAV," *Flight Dynamics*, vol. 29, no. 6, pp. 48–51, 2011.

[22] H. Chen, K. Chang, and C. S. Agate, "UAV path planning with tangent-plus-Lyapunov vector field guidance and obstacle avoidance," *IEEE Transactions on Aerospace and Electronic Systems*, vol. 49, no. 2, pp. 840–856, 2013.

[23] L. Zhu, X. Cheng, and F. G. Yuan, "A 3D collision avoidance strategy for UAV with physical constraints," *Measurement*, vol. 77, pp. 40–49, 2016.

[24] Y. C. Guo, X. X. Liu, W. G. Zhang, and Y. Yang, "3D path planning method for UAV based on improved artificial potential field," *Journal of Northwestern Polytechnical University*, vol. 38, no. 5, pp. 977–986, 2020.

[25] P. Zhao, W. Chen, and W. Yu, "Guidance law for intercepting target with multiple no-fly zone constraints," *The Aeronautical Journal*, vol. 121, no. 1244, pp. 1479–1501, 2017.

[26] O. Khatib, "Real-time obstacle avoidance for manipulators and mobile robots," *International Journal of Robotics Research*, vol. 5, no. 1, pp. 90–98, 1986.

[27] H. L. Wang, W. T. Lyu, P. Yao, X. Liang, and C. Liu, "Three-dimensional path planning for unmanned aerial vehicle based on interfered fluid dynamical system," *Chinese Journal of Aeronautics*, vol. 28, no. 1, pp. 229–239, 2015.

[28] C. Y. Tan, S. Huang, K. K. Tan, and R. S. H. Teo, "Three dimensional collision avoidance for multi unmanned aerial vehicles using velocity obstacle," *Journal of Intelligent & Robotic Systems*, vol. 97, no. 1, pp. 227–248, 2020.

[29] Y. I. Jenie, E.-J. van Kampen, C. C. de Visser, J. Ellerbroek, and J. M. Hoekstra, "Three-dimensional velocity obstacle method for uncoordinated avoidance maneuvers of unmanned aerial vehicles," *Journal of Guidance, Control, and Dynamics*, vol. 39, no. 10, pp. 2312–2323, 2016.

[30] S. X. Liu, B. Yan, T. Zhang, P. Dai, R. Liu, and J. Yan, "Three-dimensional cooperative guidance law for intercepting hypersonic targets," *Aerospace Science and Technology*, vol. 129, article 107815, 2022.

[31] B. Xya and L. Shi, "Robust intercept guidance law with predesigned zero-effort miss distance convergence for capturing maneuvering targets," *Journal of the Franklin Institute*, vol. 357, no. 2, pp. 1118–1136, 2020.

[32] P. N. Dwivedi, S. N. Tiwari, A. Bhattacharya, and R. Padhi, "Interdependent estimation and guidance with zero-effort-

miss enforcement," *IEEE Transactions on Aerospace and Electronic Systems*, vol. 55, no. 4, pp. 2012–2022, 2018.

[33] H. X. Li, H. J. Li, and Y. L. Cai, "Efficient and accurate online estimation algorithm for zero-effort-miss and time-to-go based on data driven method," *Chinese Journal of Aeronautics*, vol. 32, no. 10, pp. 2311–2323, 2019.

[34] Z. F. Xi, A. Xu, Y. X. Kou, Z. W. Li, and A. W. Yang, "Target maneuver trajectory prediction based on RBF neural network optimized by hybrid algorithm," *Journal of Systems Engineering and Electronics*, vol. 32, no. 2, pp. 498–516, 2021.

[35] Z. F. Xi, A. Xu, Y. X. Kou, Z. W. Li, and A. W. Yang, "Air combat maneuver trajectory prediction model of target based on chaotic theory and IGA-VNN," *Mathematical Problems in Engineering*, vol. 2020, Article ID 8325498, 23 pages, 2020.

[36] Y. G. Xi, *Predictive Control*, National Defense Industry Press, Beijing, 2013.

[37] X. Y. Shen, R. Y. Fang, D. Q. Li, and X. J. Wu, "A distributed adaptive moment estimation method with dynamic bound for online optimization," in *2020 IEEE 16th International Conference on Control & Automation (ICCA)*, pp. 684–689, Singapore, 2020.

[38] D. Kingma and J. Ba, "Adam: A Method for Stochastic Optimization," 2014, https://arxiv.org/abs/1412.6980.

[39] H. R. Tizhoosh, "Opposition-based learning: a new scheme for machine intelligence," in *International Conference on International Conference on Computational Intelligence for Modeling, Control & Automation*, pp. 695–701, Vienna, Austria, 2005.